



HAL
open science

X-ray Based in Situ Investigation of Silicon Growth Mechanism Dynamics-Application to Grain and Defect Formation

Hadjer Ouaddah, Maike Becker, Thècle Ribéri-Béridot, Maria Tsoutsouva, Vasiliki Stamelou, Gabrielle Regula, Guillaume Reinhart, Isabelle Périchaud, Fabrice Guittonneau, Laurent Barrallier, et al.

► **To cite this version:**

Hadjer Ouaddah, Maike Becker, Thècle Ribéri-Béridot, Maria Tsoutsouva, Vasiliki Stamelou, et al.. X-ray Based in Situ Investigation of Silicon Growth Mechanism Dynamics-Application to Grain and Defect Formation. *Crystals*, 2020, 10 (7), pp.555. 10.3390/cryst10070555 . hal-03169485

HAL Id: hal-03169485

<https://hal.science/hal-03169485>

Submitted on 15 Mar 2021

HAL is a multi-disciplinary open access archive for the deposit and dissemination of scientific research documents, whether they are published or not. The documents may come from teaching and research institutions in France or abroad, or from public or private research centers.

L'archive ouverte pluridisciplinaire **HAL**, est destinée au dépôt et à la diffusion de documents scientifiques de niveau recherche, publiés ou non, émanant des établissements d'enseignement et de recherche français ou étrangers, des laboratoires publics ou privés.



Science Arts & Métiers (SAM)

is an open access repository that collects the work of Arts et Métiers Institute of Technology researchers and makes it freely available over the web where possible.

This is an author-deposited version published in: <https://sam.ensam.eu>
Handle ID: <http://hdl.handle.net/null>

To cite this version :

Hadjer OUADDAH, Maïke BECKER, Thècle RIBERI-BÉRIDOT, Marija TSOUTSOUVA, Vasiliki STAMELOU, Gabrielle REGULA, Guillaume REINHART, Isabelle PÉRICHAUD, Fabrice GUITTONNEAU, Laurent BARRALLIER, Jean-Paul VALADE, Alexander RACK, Elodie BOLLER, José BARUCHEL, Nathalie MANGELINCK-NOËL - X-ray Based in Situ Investigation of Silicon Growth Mechanism Dynamics—Application to Grain and Defect Formation - Crystals - Vol. 10, n°7, p.555 - 2020

Any correspondence concerning this service should be sent to the repository

Administrator : archiveouverte@ensam.eu



1 Review

2 X-ray based *in situ* investigation of silicon growth 3 mechanism dynamics – Application to grain and 4 defect formation

5 Hadjer Ouaddah¹, Maïke Becker¹, Thècle Riberi-Béridot¹, Maria Tsoutsouva¹, Vasiliki Stamelou¹,
6 Gabrielle Regula¹, Guillaume Reinhart¹, Isabelle Périchaud¹, Fabrice Guittonneau², Laurent
7 Barrallier², Jean-Paul Valade³, Alexander Rack³, Elodie Boller³, José Baruchel³, Nathalie
8 Mangelinck-Noël^{1,*}

9 ¹ Aix Marseille Univ, Université de Toulon, CNRS, IM2NP, Marseille, France

10 ² Arts et Metiers Institute of Technology, MSMP, HESAM Université, F-13617 Aix-en-Provence, France

11 ³ ESRF – The European Synchrotron, CS40220, Grenoble Cedex 9, 38043, France

12 * Correspondence: nathalie.mangelinck@im2np.fr; Tel.: +33-491 28 87 37

13 Received: date; Accepted: date; Published: date

14 **Abstract:** To control the final grain structure and the density of structural crystalline defects in
15 silicon (Si) ingots is still a main issue for production of Si for photovoltaic solar cells. It concerns
16 both innovative and conventional fabrication processes. Due to the dynamic essence of the
17 phenomena and to the coupling of different scale mechanisms, the *post-mortem* study of the
18 solidified ingots gives limited results. In the past years, we developed an original system named
19 GaTSBI for Growth at high Temperature observed by Synchrotron Beam Imaging, to investigate *in*
20 *situ* the mechanisms involved during the solidification process. X-ray radiography and X-ray Bragg
21 diffraction imaging (topography) are combined and implemented together with the running of a
22 high temperature (up to 2073 K) solidification furnace. The experiments are conducted at the
23 European Synchrotron Radiation Facility (ESRF). Both imaging techniques provide *in situ* and real
24 time information on the morphology and kinetics of the solid/liquid (S/L) interface, as well as on the
25 crystal structure deformation and structural defect dynamics including dislocations during growth.
26 Essential features of twinning, grain nucleation, competition, strain building and dislocations
27 during silicon solidification are characterized and allow a deeper understanding of the fundamental
28 mechanisms of silicon crystal growth.

29 **Keywords:** Silicon; growth; grains; defects; twins; strain; dislocations; X-ray radiography; X-ray
30 topography; Bragg diffraction imaging.

32 1. Introduction

33 Current research on crystalline Si used for photovoltaic solar panels focuses on several key
34 targets from silicon purification to cell manufacturing including the silicon ingot fabrication process
35 step. Several alternative methods are proposed to optimize the Si growth process to increase the
36 production yield while reducing the costs. However, this cannot be done at the expense of the
37 crystalline quality of the final ingot as the performance of the solar cells is directly related to it. Three
38 main methods aim at mastering the initial grain nucleation and defect generation from the first stage
39 of solidification: the dendritic casting method [1, 2], the cast mono solidification (cm-Si) [3-5] and the
40 high performance multi-crystalline silicon (HP mc-Si) [6]. HP mc-Si and cm-Si techniques are both
41 used in the industry and allow producing ingots with a lower dislocation density compared to the
42 conventional mc-Si while allowing the use of low-cost casting solidification methods. In the case of
43 cm-Si, a pavement of monocrystalline seeds is placed on the bottom of the crucible in order to take

44 up the initial orientation of the seed [3]. However, cm-Si efficiencies are still limited due to the
45 presence of structural defects such as parasitic grain nucleation on the walls of the crucible [4, 7], twin
46 formation and more importantly, dislocations. The latter, can be either arranged in cellular patterns,
47 in the entire cm-Si ingot and are known as background dislocations [8] or generated on the top of the
48 seeds [9,10], at their junctions [10] on precipitates and propagate vertically along the growth direction
49 [7,11-16] generating the formation of sub-grain boundaries. HP mc-Si technique is based on a very
50 different approach aiming at obtaining small-size and uniform grains at the initial stage of
51 solidification with random angle and coherent grain boundaries [6, 17]. This results in low density of
52 dislocation clusters thanks to the interaction of blocking mechanisms by which dislocations that
53 nucleate at the beginning of the crystallization process cannot propagate further along the growth of
54 the ingot. Recent work by Stokkan et al. [17] highlighted the necessity to control the first nucleation
55 events to improve the crystalline quality. It is worth noting that in the other main process in the
56 market (Czokralski, Cz) heading at the fabrication of monocrystalline ingots, the issue of dislocations
57 and structural defects remains a main concern especially in the process of improving the method
58 (higher volumes, faster process, reusable crucibles and seeds...) [18, 19].

59 Grain boundaries and dislocations can severely limit the conversion efficiency of solar cells by
60 reducing the minority carrier lifetime [20-23]. Dislocations remain one of the most important
61 efficiency limiting defects in Si solar cells [24, 25], because they can act as preferential segregation
62 sites for impurities, ultimately reducing the carrier lifetime [11, 16, 26]. At a higher scale, sub-grain
63 boundaries and grain boundaries of high planar mismatch can be more detrimental than high
64 symmetry grain boundaries such as symmetric coincidence site lattice (CSL) twin boundaries, also
65 due to decoration by impurities [27]. Various studies show that the crystalline quality of an ingot in
66 general and the twin relationship between the grain boundary types in particular can have a
67 significant impact on the photoelectric properties [27-29]. Moreover, although it has been shown that
68 perfect symmetric $\Sigma 3$ twins have no major impact on the photovoltaic properties, the repetition of
69 twinning has important consequences for the final grain structure and distribution of
70 crystallographic orientations [30, 31]. The importance of twinning in the development of the grain
71 structure has been highlighted for very different solidification processes including directional mc-Si
72 solidification [32] and ribbon growth [33]. Another issue is to control and lower the density of strained
73 regions of the crystal structure that can be at the origin of dislocation emission during growth or
74 subsequent cooling down and solar cell fabrication processes. Recent molecular dynamics
75 simulations of silicon growth highlighted the interrelation between, strain field, dislocation
76 generation relatively to the growth direction and twin nucleation [34]. The control of the structural
77 defect formation is thus motivated by their direct impact on the PV properties. Such a control is only
78 possible if a thorough understanding of the crystal growth mechanism is achieved. The
79 understanding of the structural defect development during growth is limited by the difficulty of
80 accessing, from the *ex situ* study of the solidified ingots, to the history of defect formation and
81 interrelation. Moreover, these structural defects cover by essence a large scale range (from
82 dislocations to grains).

83 To answer these issues and key points, benchmark experiments have been proposed to
84 investigate the growth from silicon melt *in situ*. Characterisation of the solidification of an
85 undercooled levitated silicon droplet was performed using an X-ray diffractometer and by recording
86 the droplet surface image using a high speed video camera [40]. The *in situ* solidification behaviour
87 of Si droplets on silicon wafers was also characterised using IR thermal imaging [41]. Fujiwara *et al.*
88 [2,36,39,42-43] use a confocal scanning laser microscope to carry out *in situ* observations of crystal
89 growth behaviour from silicon melt by providing live images of solid-liquid interface features and of
90 the growth of grains. With this method, a detailed investigation of the Si microstructure during
91 growth has been carried out. X-ray Bragg diffraction imaging (topography) is also used to
92 characterise crystalline defects in particular [26]. More information and explanation on this technique
93 will be given in the following as this is a method of choice to characterise crystalline defects that we
94 use in our experiments. It is worth mentioning the pioneer work of Pr. Chikawa [44, 45] who
95 conducted *in situ* X-ray topography on the solidification of silicon.

96 Starting from the considerations that *in situ* characterisation of silicon growth constitutes an
97 invaluable tool to understand the crystal growth phenomena and the formation of structural defects,
98 we implemented *in situ* X-ray imaging during the solidification of silicon. The GaTSBI (Growth at
99 high Temperature observed by Synchrotron Beam Imaging) tool was developed to fulfil this
100 objective. This present paper is a review paper of our major results concerning the formation of
101 grains, twinning and competition [38, 46-53] using advanced *in situ* and complementary *ex situ*
102 characterisation methods. *In situ* X-ray imaging and methods are described in details. Our results
103 concerning dislocations and the effect of impurities [54] are not presented in details here.

104 2. Materials and Methods

105 2.1 GaTSBI tool

106 GaTSBI is a unique device that allows following in real time the solidification processes during
107 growth. It is a specially designed instrument composed of a high temperature (up to 2073 K)
108 directional solidification (DS) furnace employed in conjunction with synchrotron radiation X-ray
109 imaging techniques (Bragg diffraction imaging - topography and radiography).

110 2.1.1 Directional solidification furnace

111 The DS furnace is based on two heating graphite resistors that are inside a vacuum chamber
112 under dynamic vacuum ($\sim 10^{-6}$ mbar). The heater resistances are regulated by the DS furnace external
113 controller that uses pyrometer temperature measurements pointing on the heaters for adjustments.

114 The typical sequence used in our experiments concerning silicon solidification and in the
115 experiments analysed in the following falls down in six steps:

- 116 • Step 1 – Preheating: the sample is heated by applying the same temperature to the bottom and
117 top resistances of the furnace (isotherm conditions) up to 1373 K.
- 118 • Step 2 – Temperature gradient: a vertical temperature gradient is applied from 1373 K by
119 imposing a controlled temperature difference between both heaters. The same temperature
120 gradient is maintained until silicon melting is observed by imaging.
- 121 • Step 3 – Partial melting: the sample is partially melted and thus a seed crystal, preserving the
122 initial orientation of the sample, is kept within the field of view of the X-ray imaging.
- 123 • Step 4 – Solidification: a cooling rate is applied on both heaters until the region of the silicon
124 sample observed within the field of view is fully solidified. The same cooling rate is applied on
125 both heaters to maintain a constant temperature gradient during solidification. In some
126 particular cases, not reported in this manuscript, solidification is conducted by pulling down the
127 sample. In both cases, the solidification is directional in the upward direction due to the imposed
128 vertical temperature gradient.
- 129 • In some experiments, a new cycle is started again from step 3.
- 130 • Step 5 – Controlled cooling down: the sample is cooled down until 923 K by applying cooling
131 rates of -13 K/min and -10.4 K/min to the top and bottom heaters, respectively.
- 132 • Step 6 – Cooling down to room temperature: free cooling down takes place from 923 K as
133 temperatures below this value cannot be controlled by design of the furnace.

134 2.1.2 Crucible assembly

135 Two thin pyrolytic boron nitride (BN) plates serve as crucible material. One of the BN plates has
136 a mechanically machined slot with the dimensions of the samples. The typical sample dimensions
137 are: length 40 mm, width 6 to 8 mm and thickness about 0.3 mm. The front and back sides of the
138 sample are in contact with the crucible walls. The two BN plates are held together from the outside
139 by two Molybdenum clips so that it applies a pressure on the main surfaces of the samples. In a
140 further step, the silicon sample housed in the BN crucible, is introduced inside the DS furnace.

141
142

143 2.1.3 Origin of the silicon samples

144 The initial monocrystalline Si samples are cut from double side mechano – chemically polished
145 intrinsic (resistivity beyond 5000 $\Omega\cdot\text{cm}$) float-zone (FZ) wafers 50.8 mm, or from conventional Cz
146 industrial ingots (typical oxygen concentration: $0.5 - 1 \times 10^{18}$ at/cm³). The FZ samples provided by
147 SIL'TRONIX Silicon Technologies are produced with 9N material by the float-zone technique and
148 contain no visible dislocations at the beginning of the experiments. Oxygen and carbon
149 concentrations are below $< 10^{15}$ at cm⁻³ and metallic impurity contamination is limited to 10^{11} at/cm⁻³.

150 2.1.4 X-ray imaging

151 The GaTSBI set-up is not only a DS device but is specifically designed to allow X-rays to cross
152 the furnace windows and elements up to the sample without deleterious absorption and diffraction
153 of the incoming X-rays. The beam crosses the entry and exit vacuum chamber windows that are made
154 out of 0.5 mm thick aluminium. Additional vitreous carbon plates are positioned in the beam path
155 serving as insulation of the furnace. As a consequence, a high photon flux is needed to ensure good
156 quality imaging. This is one of the reason although not exclusive why the experiments are conducted
157 using synchrotron X-ray generated at the European Synchrotron Radiation Facility.

158 During the experiments, the sample inside the DS furnace is constantly illuminated by the X-ray
159 synchrotron polychromatic beam, which avoids variations of the heat load due to the beam. Indeed,
160 the polychromatic beam creates heat load which is minimised with filters introduced in the beam
161 before reaching the DS furnace. A compromise between minimised heat load and sufficient photon
162 flux needs to be achieved resulting in the utilisation of Al filters between 0.5 mm to 0.7 mm in our
163 experiments. On the one hand, a sufficient photon flux level is assessed qualitatively by checking that
164 the solid-liquid interface can be characterised with a counting time not higher than 1 s which is
165 requested to be able to follow its dynamic evolution during solidification. On the other hand,
166 variations of the heat load needs to be minimised for two reasons:
167 . it is sufficient to modify the thermal field inside the sample,
168 . it modifies the behaviour of the crystals used in the post-monochromator that will be described
169 in the following.

170
171 Two imaging techniques, X-ray radiography and X-ray Bragg diffraction imaging (topography),
172 are used during the steps described in section 2.1 (heating, solidification and cooling down of the
173 samples). Both imaging techniques are non-destructive.

174 175 1. X-ray radiography

176
177 In the X-ray radiography mode, the direct beam passing through the sample is used to record
178 images of the growing solid-liquid interface. A polychromatic beam is needed for the diffraction
179 imaging mode, whereas a monochromatic beam is needed in the case of X-ray radiography to increase
180 the legibility of the images. First, the polychromatic direct X-ray beam goes through the sample and
181 exits the furnace vacuum chamber. The polychromatic direct beam is then turned monochromatic at
182 a target energy, empirically determined as explained in the following, using a vertically diffracting
183 Si (111) double-crystal monochromator. Finally, images are recorded using a camera equipped with
184 a scintillator to interface X-rays with the camera matrix detector.

185 X-ray attenuation contrast is the dominating imaging modality used in the frame of this work.
186 Considering the use of synchrotron light sources, an additional modality present is related to the
187 refraction at interfaces, frequently termed propagation-based X-ray phase contrast [47, 48]. Due to
188 the rather coarse pixel sizes used and the relatively short distance between sample and detector, the
189 effect of phase contrast is not pronounced in the images shown in this work and therefore only
190 mentioned for the sake of completeness. Thus, the contrast in X-ray imaging radiographs shown here
191 is mainly due to the differential absorption of the different sample regions. The Beer-Lambert law
192 determines the absorption of a material (Equation 1). Incident monochromatic beam intensity is

193 exponentially attenuated as a function of the thickness and of the nature of the sample and of other
 194 materials crossed by the incident beam:

$$I_t = I_0 e^{-\mu_i(T,C) \cdot l} \quad (1)$$

195 where I_t is the transmitted intensity, I_0 is the incident intensity, μ_i is the linear absorption coefficient
 196 (in m^{-1}), which depends on the temperature T and on the composition C while l is the thickness. The
 197 linear absorption coefficient is a function of the density of the material.

198 As the absorption of other materials crossed by the beam is constant, the only contribution to
 199 the image contrast comes from the sample. In the case of a pure material such as silicon, a difference
 200 in transmission, and therefore a contrast in the images, is expected only from the density difference
 201 between the solid (2.33 g/cm^3) and the liquid (2.56 g/cm^3) close to the melting temperature T_m . This
 202 density difference is only 9 %. The use of monochromatic light is essential to exploit the weak
 203 attenuation contrast originating from the density difference between the solid and the liquid silicon
 204 phases in the radiography images. The choice of the monochromatic energy used for X-ray
 205 radiography is based on a compromise between an acceptable transmission and a contrast allowing
 206 to reveal the solid-liquid interface features. During our experiments, it has been empirically
 207 determined that an energy of 17.5 keV must be used, which corresponds to a transmission of 63 % of
 208 the liquid phase. However, the contrast between the solid and liquid phase is then only about 4 %.
 209 Due to the limited density difference and the compromise in energy, the solid-liquid interface is
 210 hardly distinguishable on the raw images oppositely to the case of alloys for which a higher density
 211 difference is obtained because of the presence of several phases and of solute [57]. In addition, the
 212 legibility of the images is considerably affected by the unavoidable non-uniform profile of the X-ray
 213 beam and the surface inhomogeneity of the silicon crystals in the post-monochromator. As a
 214 consequence, image processing is absolutely needed.

215 The image processing is based on the principle of pixel by pixel division and is performed using
 216 the ImageJ software [58]. By dividing two images recorded at different times, the areas that remain
 217 in the same state (liquid or solid) have the same transmission and corresponding pixel values in the
 218 images, thus the result of the division is equal to 1. As the liquid transmission is lower than the solid
 219 transmission, zones that change from liquid to solid appear in lighter grey (the result of the division
 220 is lower than 1), and zones that change from solid to liquid appear in darker grey (the result of the
 221 division is higher than 1).

222 Two types of treatment are used:

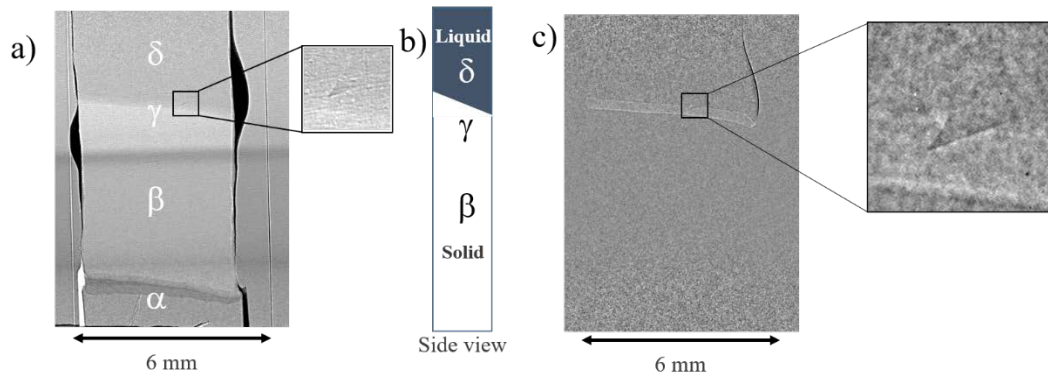
- 223 • Division by the first image taken after cooling starts:

224 For this treatment, all images of the solidification sequence are divided by a single reference
 225 image recorded just after applying the cooling rate. A typical image is shown in Figure 1.a, α , β and
 226 δ indicate the region of the regrown interface, the fully solid and liquid regions, respectively. A light
 227 grey area is observed above the fully solid zone (γ in Figure 1.a). This area corresponds to a zone
 228 constituted of solid and liquid that exists within the thickness of the sample at the level of the solid-
 229 liquid interface. This is first due to the fact that the images correspond to a projection of the sample
 230 volume hit by the beam and second to the orientation of the solid-liquid interface which is not
 231 necessarily parallel to the incident beam. An illustration of a possible solid-liquid interface side view
 232 configuration is depicted in the sketch in Figure 1.b. At the level of the solid-liquid interface region,
 233 the beam crosses at the same time solid and liquid regions which explains the grey level neither
 234 corresponding to a fully solid volume nor to a fully liquid volume.

235 This treatment allows following the evolution of the solid-liquid interface during growth.
 236 Dynamic features can be observed and the growth velocity of the solidification front can be measured.

- 237 • Division of two successive images:

238 For this treatment, each image is divided by the previous one or by an image separated from the
 239 current one by a few images only (Figure 1.c). In this case, the resulting image is less prone to noise
 240 and artefacts variations in beam intensity with time as for the first treatment. Then, sharper contours
 241 are obtained, revealing more details of the solid-liquid interface as can be seen in the close-up in
 242 Figure 1.c which shows more clearly the same grain boundary groove (close-up in Figure 1.a). The
 243 morphology of the interface and of the grain boundary grooves can thus be studied in details.



244

245

246

247

248

249

250

251

Figure 1: X-ray radiography image recorded during solidification (applied temperature gradient: 30 K/cm and cooling rate of -1 K/min applied on both heaters) from a FZ-Si seed, (a) Image resulting from the pixel by pixel division of the current image by the first image after starting the cooling down (α : seed-regrown interface, β : fully solid region, γ : solid-liquid interface region, δ : fully liquid region), (b) Sketch of the side view, (c) Image resulting from the pixel by pixel division of two successive raw images with a time interval of 3 s and close-up at the level of the interface at the same instant and position as in (a).

252

253

254

255

256

257

The radiography technique allows observing the growth of the interface, measuring the growth velocities, studying grain boundary groove evolution and the appearance of facets and twins. It provides a non-deformed image of the solid-liquid interface and of the sample. The volume projection effect needs to be taken into account for quantitative measurements (e.g. for the measurements of the facet normal growth rate discussed in section 3.1 and described in more details in [48]).

258

259

260

261

262

263

264

265

266

In the experiments presented in the following, the X-ray radiography images are recorded on detectors based on the association of a scintillator to convert X-rays and of a CCD or CMOS camera detector [60]. An optics giving a good compromise between a large field of view encompassing the whole sample width and a solidification height of about 10 mm and a sufficient spatial resolution is used. More precisely, two detectors have been used. First, a CCD camera developed at the ESRF named FReLoN (Fast Readout Low-Noise) with 2048×2048 image pixel size and an optics with 5.8 μm pixel size and a 11.9 × 11.9 mm² field of view was used. In our most recent experiments, a detector (sCMOS lens-coupled to a LuAG scintillator) 2048 × 2048 pixels with a nominal pixel size of 6.5 μm ² and a 16 bit dynamic range is used.

267

268

269

Radiography images are generally recorded every 3 s with an exposure time of 1 s which is a sufficient time-resolution to be able to characterise solidification.

270

271

2. X-ray Bragg diffraction imaging – Topography

272

273

274

275

276

277

278

279

X-ray Bragg diffraction imaging (X-ray topography) is the complementary and essential non-destructive technique used to characterize the grown crystal quality during the same experiment. When the polychromatic beam illuminates the silicon sample installed inside the solidification furnace, diffraction occurs according to Bragg's law, generating a Laue diffraction pattern in addition to the direct beam exploited for X-ray radiography. The Laue diffraction pattern is constituted of several diffraction spots related to specific lattice planes. The use of a polychromatic beam allows collecting multiple spots in a single exposure that corresponds to different crystallographic planes $\{hkl\}$ of the same grain.

280

281

282

283

284

285

The transmission mode is used i.e. the incident beam is transmitted through the sample and the diffracted beams expose a detector that is placed after the sample. Transmission mode is the only possible one in our experiments as the sample is installed inside the vacuum chamber containing the furnace. The use of a polychromatic beam allows the collection of several spots originating from multiple grains in a single exposure as well as several spots corresponding to the different crystallographic planes of a single grain.

286 Each spot provides an image of the crystal generated by the beam diffracted by the {hkl} plane
 287 family of a grain, called topograph [61]. These Bragg spots are then characterized by the hkl Miller
 288 indices of the diffracting plane and by the projection of the diffraction vector \vec{g} (reciprocal lattice
 289 vector), indicating the orientation of the spot with respect to the position of the direct beam. This
 290 technique can obviously give information on the crystallographic orientations of the grains
 291 considering the relative position of the diffraction spots, but its major output concerns the internal
 292 structure of the individual spots as they contain information on misorientations, strain fields and by
 293 extension on the presence of structural defects in general. Indeed, this is a powerful technique that
 294 can be used for the visualization of defects (dislocations, twins, domain walls, inclusions, impurity
 295 distribution) present in the crystal volume as it records their long range distortion fields and / or the
 296 strain fields associated with a macroscopic crystal deformation. However, one drawback of the
 297 technique is the complex analysis of the obtained images which are distorted images of the crystals.
 298 The origin of the contrast observed in the images is briefly explained here, the reader is directed to
 299 several references for more details [9, 59, 61-63].

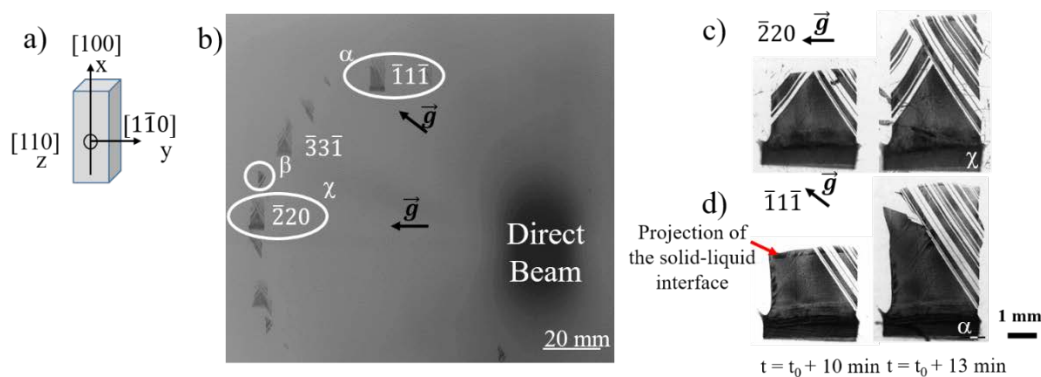
300 Due to the small beam divergence of the incoming synchrotron X-ray beam and to its large size,
 301 the whole width of our samples can be illuminated providing images exhibiting a minimum
 302 geometrical deformation effect. In our case, the diffracting volume corresponds to the width of the
 303 sample \times the height of the field of view (generally 10 mm) \times the thickness of the sample. It is worth
 304 noting that contrarily to more classical diffraction configurations, a limited number of diffraction
 305 spots can be collected during our experiments. This is due to both the distance between the sample
 306 and the diffraction pattern detector and the detector size. Indeed, although distance minimisation is
 307 always possible to some extent, some hard limits are imposed by the DS furnace vacuum chamber
 308 needed to run solidification experiments. It explains why only a few diffraction spots are recorded
 309 on the films when they are used to record the diffraction pattern.

310 A few mechanisms are responsible for the contrast and intensity on the X-ray topographs we
 311 recorded. They are structure factor contrast, orientation contrast, and the so-called "direct image"
 312 mechanism. All of them derive from diffraction theory and Bragg's law as explained for example in
 313 [64] and are evidenced in Figures 2 and 3.

314 Orientation contrast

315
 316 A particularly clear illustration of the orientation contrast is given in the presence of twins
 317 observed in our experiments (Figures 2 and 3) [46, 51].

319



320

321 **Figure 2:** X-ray diffraction images (topographs) recorded during solidification (applied temperature
 322 gradient: 30 K/cm and cooling rate of -1 K/min applied on both heaters at t_0) from a FZ seed, (a)
 323 Crystallographic orientation of the seed, (b) Laue pattern recorded at the end of solidification showing
 324 the diffraction spots in the field of view. Images of the (c) $\bar{1}1\bar{1}$ and (d) $\bar{2}20$ topographs recorded at
 325 two instants during solidification.

326 Indeed, in the case of twinning during growth, the diffraction images are very different
 327 depending on the diffraction spots as can be seen in Figure 2. A typical hatched aspect is observed
 328 for the diffraction spots corresponding to {hkl} family planes as can be seen in Figure 2.b (e.g. α , β
 329 and χ). The diffraction spot χ ($\bar{2}20$) shows a diffraction spot corresponding to {hkl} family planes
 330 which are not common with twinned grains that developed on both right and left hand sides of the
 331 sample (Figure 2.c). The complementary image corresponding to the twinned grains on the left
 332 (Figure 2.b β) is found at another position of the diffraction pattern, whereas the diffraction spot α
 333 ($\bar{1}\bar{1}\bar{1}$) includes the diffraction patterns of the common family planes of the central main grain and of
 334 the twinned grains on the left (Figure 2.d). This is a particularly important element to be kept in mind
 335 when analysing the topographs. Indeed, the observation of a single diffraction spot can be
 336 misleading. This is one of the reasons why several diffraction spots must be analysed to be able to
 337 conclude.

338 Orientation contrast can be also produced, for instance when the sample displays sub-grain
 339 boundaries. For a monochromatic beam, the region corresponding to a {hkl} plane family is imaged
 340 at a position given by the Bragg's law. Regions of different crystallographic orientations are not seen
 341 simultaneously on the diffraction image and appear as non-illuminated (white) zones. When a
 342 polychromatic beam is used, the misoriented regions are all in diffraction position simultaneously,
 343 but for different wavelengths. The images diffracted by neighbouring sub-grains can exhibit a
 344 contrast associated with geometrical local superimpositions or separations of the diffracted beams on
 345 the topographs, according to the dimensions of the misoriented zone and to the value of the
 346 misorientation.

347 Crystalline defects such as precipitates, dislocations and impurities, act on the diffraction
 348 process through their associated effective misorientation angle variation $\delta\theta_m(\vec{r})$, which can be
 349 approximated by Equation 2 [59, 63]:

$$\delta\theta_m(\vec{r}) = \frac{\delta d}{d}(\vec{r})\tan\theta_B \pm \delta\theta(\vec{r}) \quad (2)$$

350 where θ_B is the Bragg angle, $\frac{\delta d}{d}(\vec{r})$ is the local relative change of the lattice parameter and
 351 $\delta\theta(\vec{r})$, the local change in crystallographic orientation. The double sign has to be chosen to take into
 352 account the effect of the deformation on the Bragg angle (decrease or increase of its value). This
 353 effective misorientation corresponds to the strain field generated by the defect, which is at the origin
 354 of Bragg diffraction of components of the incident beam that do not participate to the diffraction for
 355 the perfect crystal matrix [38, 62]. This is the "direct image" mechanism that leads, in the X-ray low
 356 absorption case we are concerned with, to supplementary diffracted intensity associated to distorted
 357 regions. Andrew Lang developed this technique and revealed dislocations in silicon in his pioneer
 358 work [61]. The diffraction imaging technique was also used by Oriwol *et al.* [26] to study dislocations
 359 and the formation of sub-grain boundaries *ex situ* in Si ingots. Indeed, diffraction imaging applied to
 360 silicon crystals have proven to give unique insights into the evolution of dislocations [65, 66] and
 361 cracks [67]. As can be understood from the above, one of the main advantages of diffraction imaging
 362 is that it can reveal low scale structural defects like dislocations on wide field images encompassing
 363 complete crystals as shown for example for diamonds by Burns *et al.* [62] and for Si [38, 53, 68].
 364

365 An illustration is given in our work on Figure 3.c. In this topograph corresponding to the
 366 $\bar{1}\bar{1}\bar{1}$ diffraction spot and recorded during the solidification from a silicon FZ seed (orientation Figure
 367 3.a), black contrasts revealing deformation of the crystal structure are present at several places.
 368 Moreover, the deformation due to single dislocations can be clearly revealed in the seed and above
 369 the seed-regrown interface.

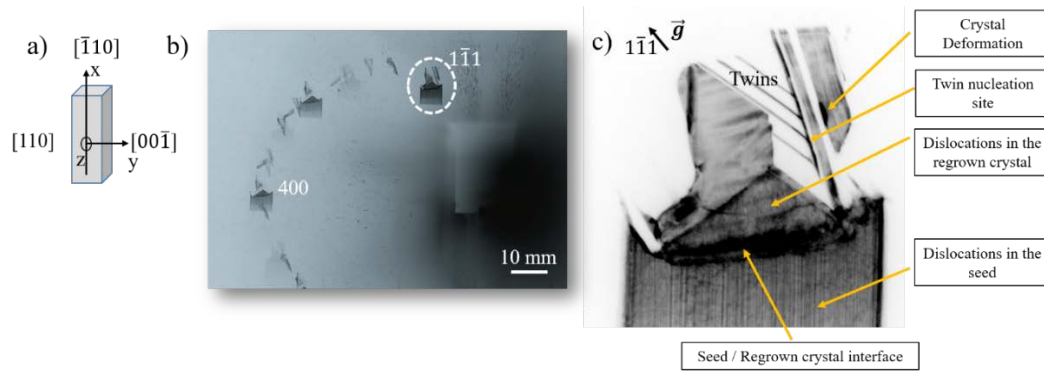


Figure 3: X-ray diffraction imaging (topography) during solidification (applied temperature gradient: 30 K/cm and cooling rate of -1 K/min applied on both heaters) from a FZ seed, (a) crystallographic orientation of the seed, (b) Laue pattern showing the diffraction spots recorded at the end of solidification in the field of view, (c) topograph of the $1\bar{1}1$ diffraction spot during solidification.

Importantly, if the strain field created around a defect is related to particular crystallographic orientations, it is not visible in all diffraction spot images (topographs). Indeed, if the displacement vector is perpendicular to the diffraction vector, the defect is not visible on the topograph. This is the case of dislocations whose image is extinct for the diffraction spots corresponding to diffraction vectors perpendicular to the Burgers vectors as also seen in TEM investigations [69, 70]. On the one hand, this means that the absence of a dislocation strain field on a single diffraction spot does not mean that no dislocations are present. Depending on the dislocation character, at least two diffraction spots with different diffraction vectors perpendicular to each other must be analysed before being able to conclude on the presence or not of dislocations. On the other hand, extinction is a powerful method to retrieve the Burgers vector direction as explained in details for example in [71].

2.1.5 Dynamic evolution

Another main originality of the experimental configuration we use is that several Laue patterns or topographs are recorded during a solidification experiment [38, 46, 72]. Then, it is possible to obtain sequences showing the evolution with time of the Laue pattern and of the topographs during the development of the grains. Such sequences allow a better understanding of the competition between the grains and of the occurrence of the twinning phenomenon. At the same time, the dynamics of the formation and evolution of defects as dislocations is followed during growth. The study of the growth of individual grains is then possible, along with the development of strain fields produced in the crystal structure by the structural defects. The combination of both imaging techniques and of the DS furnace provides complementary dynamic information about crystal growth and competition and about the crystal structure deformation.

Up to 2018, both *in situ* and real time X-ray imaging techniques: X-ray radiography and Bragg diffraction imaging (topography) were used alternately during growth. In this configuration, the different diffraction spots are collected on photographic films positioned after the furnace regularly during the experiment thanks to a specially designed device. X-ray diffracted beams are successively recorded on X – ray sensitive films (AGFA Structurix D3-SC, 17.6×12.5 cm²) positioned at a distance about 300 mm from the sample. The exposure time used to record the diffraction patterns is usually of 0.5 s. In this configuration, radiographs and topographs are thus recorded alternately.

In 2018, we implemented together with the ESRF ID19 team a solution to record simultaneously radiographs and diffraction images (topographs). In this configuration, a scientific CMOS camera lens-coupled to a LuAG scintillator (commercial Ce-doped Lu₃Al₅O₁₂, Crytur company – Czech Republic) is used to record the images of one of the diffraction spots (topograph). The camera has 2048 × 2048 pixels with a nominal pixel size of 6.5 μm² and a dynamic range of 16 bit. It is coupled with a ×1.5 optic to decrease the pixel size to 4.3 μm². In this new configuration, images recorded from both modes are fully synchronised. The image acquisition rate is of 2 frames per second in experiments reported in [53] which is sufficient to follow the solidification front of the samples. The

411 choice of the diffraction vector of the recorded spots and the alignment of the camera with respect to
412 the sample face is an important aspect because it influences the appearance and the information that
413 can be revealed from the recorded topographs. Ideally a spot with a high intensity induced by the
414 crystal plane structure factor should be chosen to better reveal defects. A detailed description of the
415 equipment and imaging methods and configurations (alternate or simultaneous recording) can also
416 be found in our previous publications [50, 51, 53].

417 2.2 *Ex situ* complementary investigations

418 After the last melting – solidification cycle, the samples are cooled down to room temperature
419 and removed from the GaTSBI furnace. *Ex situ* electron backscatter diffraction (EBSD) measurements
420 are performed after mirror polishing down to 1 μm diamond paste using a FEG-SEM JEOL JSM 7001F
421 equipped with a HKL Nordlys camera with either a 7 μm or a 0.7 μm step size depending on the
422 studied area. In order to depict the three – dimensional orientation of the crystals in the sample,
423 inverse pole figure (IPF) orientation maps are generated with respect to the three space directions:
424 normal to the sample surface (z), transverse direction (y) and in the growth direction (x). Moreover,
425 the coincidence site lattice map (CSL) is reconstructed to evidence the grain boundaries with a special
426 character. In this paper, $\Sigma 3$ $\langle 111 \rangle$ (red colour in the maps), $\Sigma 9$ $\langle 110 \rangle$ (blue) and $\Sigma 27a$ $\langle 110 \rangle$ (yellow)
427 twin boundaries labelling refer to rotations around $\langle h k l \rangle$ axis that satisfy the misorientation ranges
428 given by the Brandon criterion, $(60 \pm 8.66)^\circ$, $(38.94 \pm 5)^\circ$ and $(31.58 \pm 2.89)^\circ$, respectively. Additionally,
429 the grain orientation spread (GOS) map is extracted as well from the EBSD results. The GOS map is
430 constructed by calculating the difference between the orientation of each pixel in the grain and of the
431 grain average orientation to evidence the more distorted areas within a grain structure. A colour code
432 is used to depict the grains without deformation (perfect Si crystal appears in blue) and having an
433 average crystal structure deformation (red colour for the highest deformation).

434 3. Results and discussion

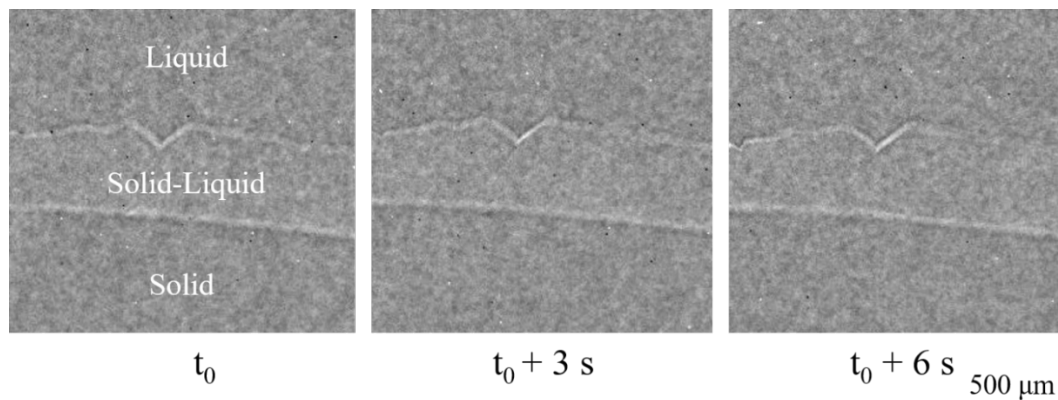
435 3.1. $\{111\}$ facet growth and undercooling

436 Theoretical models of the $\{111\}$ facet growth laws exist [73, 74] and are related to the
437 undercooling at the level of the $\{111\}$ facets. However, the orders of magnitude of the undercooling
438 values for the corresponding laws are very different, so that experimental validation is needed.
439 Moreover, directional solidification is widely used for the fabrication of multi-crystalline ingots so
440 that the knowledge of $\{111\}$ facet dynamics needs to be known during DS. Moreover, it constitutes a
441 critical building block to develop predictive and quantitative models [75-77]. Moreover, the presence
442 of $\{111\}$ facets at the solid-liquid interface leads to the occurrence of twinning ultimately competing
443 with the central grain growing from the seed as will be discussed in the following. It is thus essential
444 to understand their formation mechanism and the undercooling at their level which gives conditions
445 for twin nucleation. Our main objective has thus been to determine the contribution of the
446 undercooling of the $\{111\}$ facets at the solid-liquid interface during Si directional solidification. $\{111\}$
447 facet growth laws are derived and then compared with theoretical growth models reported in the
448 literature.

449 At the level of the solid-liquid interface, $\{111\}$ facets appear at the sample edges and in grain
450 boundary grooves. Grain boundary grooves are formed due to the encounter between a grain
451 boundary and the solid-liquid interface [78]. From the theory [79], grain boundary grooves can be
452 either faceted/faceted, faceted/rough or rough/rough depending on the crystallographic
453 orientation of the adjacent grains. Experimentally, we are able to characterize faceted/rough and
454 faceted/faceted grain boundary grooves [48, 80] with a large prevalence for the faceted/faceted
455 configuration. However, conclusions concerning the predominance of one or the other grain
456 boundary groove type cannot be drawn from these observations as rough/rough grain boundary
457 grooves are expected to correspond to lower undercoolings compared to faceted/faceted ones and
458 thus to smaller depth that can then fall below the spatial resolution used in these experiments.

459 Whatever conditions, facets observed in our experiments are always {111} facets as foreseen in
 460 silicon [81]. It was checked by determining the crystallographic orientation of the grains and their
 461 relative {111} facet orientation. In order to determine {111} facet growth laws, the grain boundary
 462 grooves observed at the solid-liquid interface (e.g. in Figures 1 & 4) have been geometrically
 463 characterized by their angle and depth in the case of an ideal faceted/faceted groove [82]. The
 464 geometrical parameters of the grain boundary grooves can be measured directly on the radiography
 465 images collected during solidification (Figures 1 & 4). The kinetic parameters, growth velocity of the
 466 interface and normal growth velocity of the groove facets are also measured thanks to the time-
 467 resolved observation of the solid-liquid interface evolution.

468 When comparing the growth rate of the global solid-liquid interface to the {111} facet growth
 469 rates, it appears first that the growth rates of the {111} facets both inside the grooves and at the edges
 470 are smaller than the one of the global solid-liquid interface. This is expected because of the slower
 471 kinetics of the {111} planes compared to the other crystallographic orientations so that they are
 472 lagging behind other growing orientations and generally behind the global solid-liquid interface [47].
 473 A major consequence is that the undercooling is higher in the groove and at the level of the edge
 474 facets compared to the one at the level of the global solid-liquid interface. This favors nucleation
 475 events inside grooves and at the edge facets that are indeed often observed in real time during our
 476 experiments.
 477



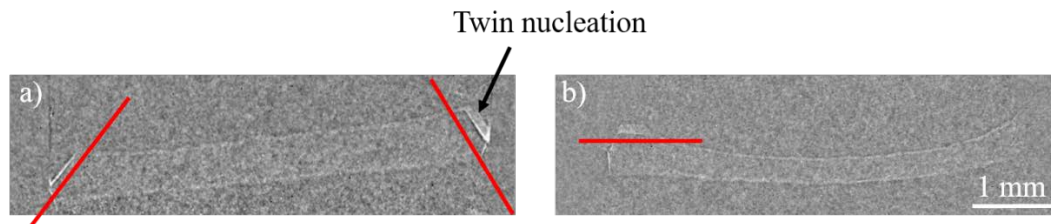
478

479 **Figure 4:** X-ray radiography images recorded during solidification, applied temperature gradient: 30
 480 K/cm and cooling rate = -1 K/min applied on both heaters. Typical faceted / faceted grain boundary
 481 groove revealed by division by successive images.

482 The dynamics of a faceted / faceted groove during solidification can be seen for example in
 483 Figure 4. Both facets grow at the same growth rate as can be concluded from the constant angle and
 484 orientation of the groove. This conclusion is also sustained by the X-ray radiography images contrast
 485 (Figure 4.c). The white areas on the facets evidence the new grown solid between two successive
 486 images because of the image processing performed as explained in the experimental section. These
 487 white regions have the same thickness on both facets which indicates that both facets grow at the
 488 same rate. This is observed in all studied cases for faceted/faceted grain boundary grooves.

489 The maximum thermal undercooling inside a grain boundary groove can be calculated knowing
 490 the local temperature gradient and the maximum grain boundary groove depth. Details of the
 491 calculations can be found in [48]. The measured maximum undercooling has been thus calculated
 492 inside grain boundary grooves for several experiments with seeds oriented along $\langle 100 \rangle$, $\langle 111 \rangle$ and
 493 $\langle 110 \rangle$ directions. In all cases, the maximum undercooling inside the grain boundary groove is found
 494 to be always lower than 1 K ranging from 1×10^{-1} to 4×10^{-1} K and adds to the solid-liquid interface
 495 undercooling [47]. Eventually, the mean facet velocity evolution as a function of the additional
 496 undercooling inside the grain boundary grooves can be obtained.

497 Moreover, {111} facets are also observed at the level of the solid-liquid interface at the sample
 498 edges as can be seen in Figures 1.c and 5. The same procedure is applied to the {111} facets at the
 499 edges of the samples except that there is only one facet to consider in this case.



500
501
502
503

Figure 5: X-ray radiography images of the solid-liquid interface during growth with {111} facets at both edges of the sample for the experiments: (a) same experiment as in Figures 2 and 6.a, (b) same experiment as in Figure 6.c. Red lines indicate the traces of {111} planes.

504
505
506
507
508
509
510
511
512
513
514

At the level of the edge facets, the measured maximum undercooling is again always lower than 1 K. However, higher values (ranging from 2×10^{-1} to 8×10^{-1} K) compared to the undercooling inside grain boundary grooves are measured at the edges. This result is significant because the same evolution is obtained for several samples and for both grooves at the edges independently from possible sample particularities. The higher undercooling measured at the level of the edge {111} facets has a significant impact on the grain structure obtained at the end of solidification as it increases the nucleation probability during growth at the level of the edge facets. This is clearly confirmed by the grain structure obtained in the samples at the end of the experiments for which twin nucleation is frequent at the far edges of the facets (Figure 6). This major contribution of twins nucleating on edge {111} facets to grain competition and final grain structure was previously reported [7, 38] and was observed repeatedly in our experiments.

515
516
517
518
519
520
521
522
523

The undercooling inside the grain boundary grooves and at the level of edge facets is always lower than 1 K relatively to the global solid-liquid interface which is far smaller than the undercooling values predicted by the bi-dimensional laws (several K) for the growth rates measured during these experiments. As a consequence, bi-dimensional nucleation growth mechanism [73] can be excluded. The experimental results concerning {111} facets kinetics in our experiments can only be compared favourably to the theoretical law corresponding to a growth mechanism eased by the presence of dislocations proposed by Voronkov [74]. This is in agreement with the fact that dislocations are expected to be easily generated during silicon growth and found emerging at the level of facets as shown for example in [38, 83] and as can be seen in Figure 3.

524

3.2 Twinning during solidification:

525
526
527
528
529
530
531
532
533

As discussed in the introduction, the crystalline quality of the ingot and the grain boundary types, in particular the twin boundary characteristics, can have a significant impact on the photoelectric properties [22, 27]. It has been shown that perfect symmetric $\Sigma 3$ twins have no major impact on the photovoltaic performance. However, the repetition of twinning has important consequences for the final grain structure and distribution of crystallographic orientations [31]. Indeed, the importance of twinning in the development of the grain structure has been highlighted for different solidification processes ranging from directional solidification [84] to ribbon growth [33, 85-86]. In the past few years, we studied rather extensively twin formation, growth and its consequences on the final grain structure and defect formation in general [38, 46, 48, 49, 51, 53, 87].

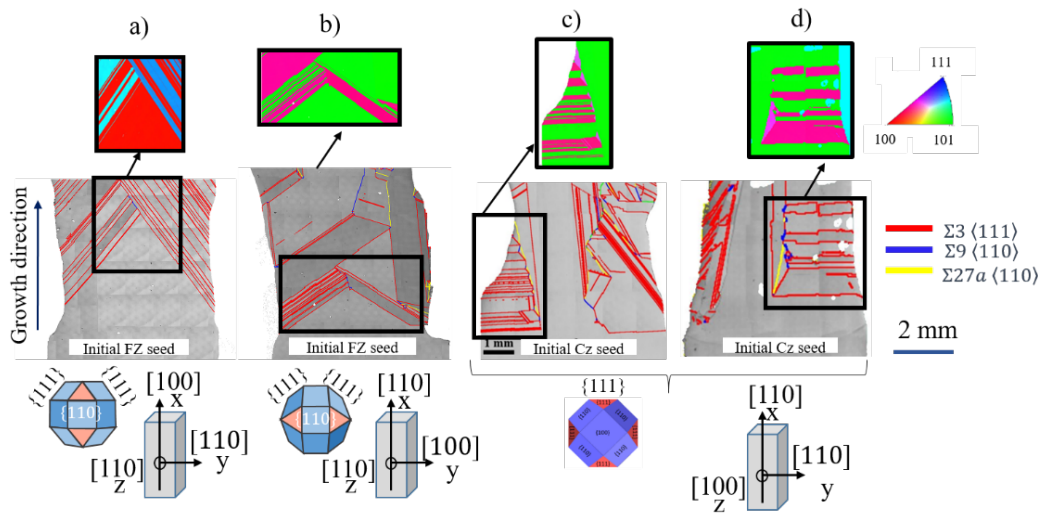
534

3.2.1 Twin nucleation

535
536
537
538
539
540
541
542

Four typical final grain structures of samples solidified from a seed in the GaTSBI DS furnace are shown in Figure 6. The coincidence site lattice maps (middle line in Figure 6) are shown in order to reveal the grain boundary character and in particular the twin boundaries. These samples are solidified from float-zone (FZ) monocrystalline seeds (Figures 6.a and b) and from Czochralski (Cz) seeds (Figures 6.c and d) after partial melting of the seed. The samples are solidified from seeds with different crystallographic orientations in the growth direction (Figure 6 bottom line). In all cases, side twins develop at the edges from {111} facets and compete with the main central grain issued from the seed, as it was also observed by Trempa et al. [7] in a systematic study. The fact that the behavior of

543 FZ and Cz seeds is comparable suggests that the presence of oxygen (typically: $0.5 - 1 \times 10^{18}$ at/cm³ in
 544 Cz ingots compared to $< 10^{15}$ at/cm³ in FZ ingots) is not a predominant factor for the twin nucleation.



545

546 **Figure 6:** EBSD measurements revealing the grain structure and twin boundaries after growth and
 547 cooling down in samples grown from monocrystalline seeds. Applied temperature gradient: 30 K/cm
 548 and cooling rate applied on both heaters (a) -1 K/min (same experiment as in Figures 2, 8.a-b and 9),
 549 (b) -1 K/min, (c) -0.2 K/min (same experiment as in Figures 7.b, 8.c-e), (d) applied temperature
 550 gradient: 20 K/cm and cooling rate: -0.2 K/min (same experiment as in Figure 7.a). Top: Inverse Pole
 551 Figure (IPF) map along the growth direction. Middle: CSL (Coincidence Site Lattice) map. Bottom:
 552 Seed orientation and {111} planes.

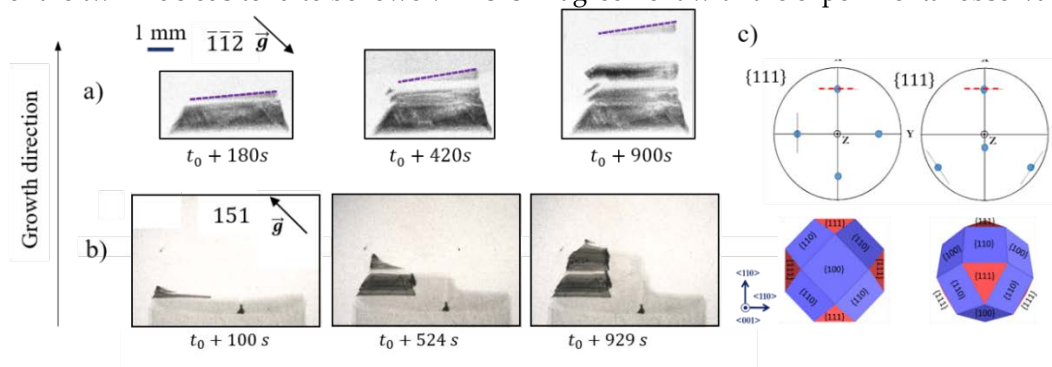
553 Figures 5.a and 5.b correspond to a snapshot at one instant during solidification showing the
 554 solid-liquid interface of samples in Figures 6.a and 6.c, respectively. The *in situ* X-ray radiography
 555 images (Figure 5) reveals that the solid-liquid interface is smooth during growth under these
 556 conditions for both Cz (Figure 5.a) and FZ (Figure 5.b) seeds. No destabilization of the interface can
 557 be observed in all cases when Cz or FZ seeds are used. Interface destabilization has only been
 558 observed in the presence of Cu impurities as reported in [54].

559 Despite the global smooth interface, {111} facets can be clearly seen on the X-ray radiography
 560 images at the edges of the sample (Figure 5). It was verified that they correspond to the projection of
 561 {111} facets by determining the corresponding pole figures using the measurements performed by
 562 EBSD. The {111} facet orientation is highlighted by the red lines on Figure 5. Twin nucleation takes
 563 place regularly on these {111} facets as can be seen for example on Figures 5.a (right) and 5.b (left). A
 564 video of radiograph images showing the dynamic evolution of the solid-liquid interface during the
 565 experiment corresponding to Figures 2, 5.a and 6.a is provided as supplementary material. It
 566 evidences, twin nucleation at the {111} edge facets and the formation of grain boundary grooves at
 567 the solid-liquid interface due to the subsequent grain competition.

568 Diffraction spot images collected at different times during the solidification of the two samples
 569 (corresponding to the experiments and grain structure in Figures 6.c and d) are shown in Figure 7.
 570 The diffraction spots in Figure 7.a display the twinning zone at the right side of the sample in Figure
 571 6.d, whereas the diffraction spots in Figure 7.b display the twinning zone at the left side of the sample
 572 in Figure 6.c. The purple dotted line is added in Figure 7.a to indicate the corresponding solid-liquid
 573 interface shape as observed in the radiographs. It is worth reminding that diffraction imaging shows
 574 only the crystalline solid areas. The observation of the upper part of the diffraction spots shows that
 575 the twin nucleation occurs at the edges of the samples at the solid-liquid-vacuum-crucible phase line
 576 as also seen in the radiographs (Figure 5 and supplementary material). A sudden increase of the solid
 577 height at the solid-liquid interface is observed at the instant of each new twin nucleation on the time-
 578 resolved radiography images. From these height differences a value of the nucleation undercooling
 579 has been estimated and it ranges from 0.1 K to 0.5 K for the experiment corresponding to Figures 5.b,

580 6.c and 7.b, which is also consistent with the results reported in section 3.1. These measurements
 581 confirm that the undercooling measured in grain boundary grooves and at the edges are sufficient
 582 for twin nucleation on the {111} facets.

583 A 3D model was proposed by Jhang *et al.* [88] to determine the nucleation probability at the level
 584 of {111} facets. This model was specifically applied to several of our experimental cases. The twin
 585 grain nucleation probability was found to be higher when there is a contact between the {111} facet
 586 and crucible walls. This is generally the case in our thin sample configuration. Additionally, the
 587 authors showed that the attachment energy and the contact area with crucible walls are the key
 588 factors for the heterogeneous nucleation of twins. Low attachment energy and lower contact area
 589 concur to the highest twinning probability on the {111} facets. When applied to our experimental case,
 590 it is found that twin grain nucleation probability is higher at the sample edge {111} facets compared
 591 to the ones situated in grain boundary grooves, where the attachment energy and the bottom contact
 592 area of the twin nucleus tend to be lower. This is in agreement with the experimental observations.



593
 594 **Figure 7:** Image sequence of diffraction spot images – topographs corresponding to twinning zones
 595 (a) twinning zone corresponding to the right side of sample Figure 5.d. The purple dotted line
 596 correspond to the solid-liquid interface, (b) twinning zone corresponding to the left side of sample
 597 Figures 5.c and 6.b, (c) stereographic projections of the {111} planes of the seed (left) and the first
 598 twin (right) with both horizontal projections for the experiment in (b) and the corresponding 3D
 599 representation of the plane arrangements (below).

600 Moreover, the twin growth rate at the nucleation instant (about $15 \mu\text{m/s}$) exceeds the one of the
 601 global solid-liquid interface ($2 \mu\text{m/s}$). The consequence is that the twin grains that nucleate on the
 602 edges grow vertically very fast and in advance compared to the global solid-liquid interface inducing
 603 the triangular images recorded during solidification on the topographs. Such a triangular shape of
 604 the twins growing at the solid-liquid interface has been repeatedly observed in our experiments
 605 during solidification. When the crystal arrives at the liquidus isotherm position, stabilization of the
 606 growth rate is observed until the global solid-liquid interface arrives at the liquidus. As a subsequent
 607 step, a growth rate plateau is measured, after which the next twin nucleation can take place [38]. The
 608 nucleation of the twin and growth upwards along the directional solidification direction goes along
 609 with the propagation of the twin grains towards the center as revealed by the topographs (Figure 7).

610 A main result of our work is that only $\Sigma 3$ type twinned grains nucleate during growth. This
 611 conclusion can only be drawn because we are able to monitor the growth *in situ* with X-ray imaging.

612 3.2.2 Successive Twinning

613 The successive twinning zones are immediately identifiable on ingots after solidification. It is
 614 evidenced on both the grain structure EBSD maps (Figure 6, upper line) and diffraction images for
 615 example on Figures 2, 3 and 7. The successive twinning zone is observable by the alternation of two
 616 crystallographic orientations (Figure 6) on the EBSD maps and by the striped/hatched aspect of the
 617 topographs (Figures 2, 3 and 7). Only two crystallographic orientations alternate and they share a
 618 common {111} plane. The fact that crystallographic orientations are found successively can be
 619 explained by the orientation of both seed and first twin grain. The stereographic projection of {111}
 620 planes of both the seed and first twin grain (green and pink color in Figure 5.c, respectively)

621 corresponding to Figures 6.c and 7.b is shown in Figure 7.c. These two stereographic projections are
622 sufficient to describe the grains of the entire twinning zone because only two crystallographic
623 orientations are successively repeated. The seed (Figure 7.c left) presents four {111} planes, two with
624 a vertical projection parallel to the growth direction, and two {111} planes presenting a horizontal
625 projection perpendicular to the growth direction and facing the liquid. The first nucleus initiated at
626 the left edge of the sample nucleates on the {111} facet having a horizontal projection (Figure 7.c right).
627 This is confirmed by the existence of a common {111} plane between the seed and the horizontal twin.
628 Then, as a subsequent step, the first twin has only one {111} plane presenting a horizontal projection
629 perpendicular to the growth direction and facing the liquid. The next $\Sigma 3$ twin nucleating on this {111}
630 facet has the same orientation as the initial seed so that the crystallographic orientation is alternately
631 retrieved.

632 3.2.3 Twin growth

633 Once a twin nucleus appears at the sample edges on a {111} facet, it grows laterally as shown by
634 the *in situ* radiography and topography images. Twin grains grow towards the central part along
635 their respective {111} facets until they meet the grain that took over from the seed or other twinned
636 grains (Figure 6). Indeed, the progress of the pristine grain issued from the seed can be stopped by
637 the competition with twinned grains as for example in Figures 6.a and b. This is in fact totally
638 controlled by the relative orientation of the seed that determines the orientation of the {111} facets
639 initiating twinning as can be seen on the sketch showing the {111} facet orientations of the seeds in
640 Figure 6 (bottom line) and as studied by Trempa *et al.* [7].

641 3.3 Grain competition and higher order twin boundaries

642 The encounter of twinned grains with other grains creates grain boundaries, which leads to the
643 formation of grain boundary grooves at the solid-liquid interface (see as well supplementary
644 material). The grain boundary type formed is directly linked to the adjacent grain orientations. As
645 seen above, the $\Sigma 3$ type twinned grains are the only ones to nucleate during growth so, higher order
646 twin boundaries such as $\Sigma 9 \langle 110 \rangle$ and $\Sigma 27a \langle 110 \rangle$ are in all the experimental cases (FZ or Cz seeds)
647 only the result of grain encounter and competition. A statistical analysis on the percentage of the
648 different types of twin boundaries in relation to the total number of twin boundaries was obtained
649 from EBSD measurements after the last solidification experiment on several samples from FZ seeding
650 to exclude the influence of impurities. It is clearly seen that the majority of twin boundaries are of $\Sigma 3$
651 type (typically more than 90 %). Whereas the proportion of $\Sigma 3$ twin boundaries is regularly retrieved
652 for these pure seed samples, the proportion of higher order twin boundaries depends on the growth
653 and nucleation events. As the samples grow, more $\Sigma 3$ twin grains nucleate so that encounters are
654 more likely to occur increasing the amount of higher order twin boundaries. The experimental results
655 shown in Figures 2 and 6.a have been recently simulated using a 3D cellular automaton model of the
656 grain structure [77]. The dynamics of {111} facets and the nucleation, growth and competition of
657 grains in twin relationship could be modelled and compared successfully to the experiments. The
658 application of this model to larger scale ingot solidification is foreseen. It is worth noting that a
659 different behaviour was observed in samples containing higher levels of impurities for which
660 although the predominance of $\Sigma 3$ twin grains is still maintained, other grain nucleation events can
661 take place [54].

662 3.4 Strain building during growth

663 The study of local strain development during growth (deformation) is of great importance as
664 local deformations can lead to the formation of dislocations, which are major defects affecting the
665 material electrical properties as seen in the introduction. On the one hand, dislocations can develop
666 during the cooling down of the sample following the solidification due to the Alexander– Haasen
667 model [89]. On the other hand, the local nucleation of dislocation clusters is expected to take place
668 during crystal growth [90, 91].

669 Before presenting results on strain building, it is important to specify that during the heating
670 segment of the experimental procedure, dislocations appear in the sample as described in [72] and
671 remain in the seed kept after partial melting. During solidification, these dislocations develop,
672 usually along the growth direction and can encounter grain boundaries. Dislocations can be stopped
673 and accumulate, unless they are able to cross-slip at the level of a grain boundary which is most likely
674 to occur at $\Sigma 3$ type twin boundaries because of the presence of a $\{111\}$ possible gliding plane [38]. For
675 example, in nickel [92], coherent $\Sigma 3$ twin boundaries act as effective barriers to slip except in the case
676 of screw dislocations which can direct or cross slip across the boundary using the $\{111\}$ boundary
677 plane itself. During growth, dislocations can propagate or cross slip and propagate along the $\{111\}$
678 planes until they reach a free surface or meet another interface.

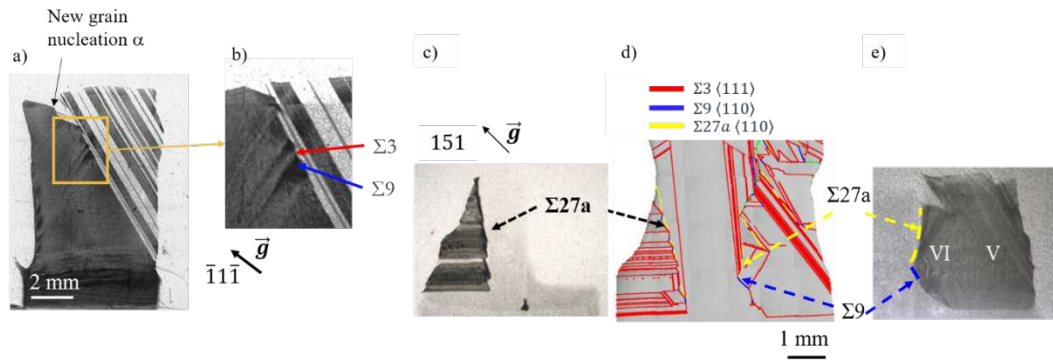
679 3.4.1. Strain and $\Sigma 3\{111\}_{1,2}$ twins

680 Strain is observed at the location of twin nucleation as can be clearly seen on the topographs in
681 Figures 2.d and 3. It is revealed by the increased black contrast observed at the location of twin
682 nucleation. Although the apparition of these contrasts is concomitant to twin nucleation and
683 beginning of growth, it is not possible up to determine if the deformation is present just before or just
684 after the nucleation event. This is one aspect that will be studied in more details in the future. A video
685 of topographs showing twinning and strain formation during solidification in the experiment
686 corresponding to Figure 3 is provided as supplementary material. As explained in Section 2,
687 dislocations can be clearly evidenced as well as their interaction with twin boundaries. Besides, a
688 black contrast observed at the level of twin nucleation (Figure 2) is retrieved on the projected image
689 of the solid-liquid interface. It can be associated to the gliding of dislocations along the $\{111\}$ facets
690 that exit at the solid-liquid interface confirming that dislocations can in some cases glide along these
691 planes as also seen in [38].

692 3.4.2. Strain building due to competition

693 Local strain heterogeneities are also created due to grain competition. This is clearly evidenced
694 in the topographs shown in Figure 8. Comparing the CSL map (Figure 6.a) with the respective
695 diffraction image (Figures 8.a and b), it can be concluded that no local strain accumulation occurred
696 at the level of $\Sigma 3$ twin boundaries except at the nucleation location as discussed above. On the
697 contrary, a localized strain field is characterized at the position of $\Sigma 9$ twin boundaries as evidenced
698 by the black contrast on the topograph (Figure 8.b). This is expected as in the case of $\Sigma 9$ twin
699 boundaries, cross slip is unlikely. Only the dislocations having the Burgers vector directions of a
700 common rotation axis $\langle 110 \rangle$ to build a symmetric grain boundary can cross slip; for other rotation
701 axes, cross slip is not possible. As a consequence, dislocations and strain accumulate at the level of
702 the $\Sigma 9$ twin boundary. The same observation is made each time $\Sigma 3$ and $\Sigma 9$ twin boundaries are
703 formed due to competition for all successive twins. Moreover, it is worth noting that the strain created
704 by the grain competition seems to propagate over longer distances in the samples. This can be seen
705 in the few millimeters wide expansion of the black contrast from the competition zone on the right
706 side of the sample (Figure 8.b).

707
708



709

710

711

712

Figure 8: (a) Topograph for the experiment in Figures 2, 5.a and 6.a, (b) Close up at the level of competing twin grains, (c) topograph for the experiment in Figures 5.b, 6.c and 7.b-c, (d) corresponding coincidence site lattice map and (e) topograph of a grain on the right side.

713

714

715

716

717

718

719

720

721

722

723

This observation is not a single observation corresponding to a particular experiment but was repeatedly observed during solidification. In successive twinning configuration, due to the alternated twin crystallographic orientations, the same grain boundary types are retrieved alternately. In the experiment presented in Figures 8.a-b, $\Sigma 3$ and $\Sigma 9$ twin boundaries are formed and are observed in sequence which means that local deformations are built successively according to the grain boundary type. On the experiment shown in Figures 8.c-e, $\Sigma 3$ and $\Sigma 9$ twin boundaries are also formed and are observed in sequence as well as $\Sigma 27a$ type twin boundaries. For the later grain boundary type, high strained zones (Figures 8.c-d) are created which could be due to the accumulation of already present dislocations that cannot cross slip or to the emission of dislocations from imperfect grain boundaries from the crystallographic point of view. Dislocation emission is clearly observed at the level of a $\Sigma 27a$ type twin boundary (Figure 8.e).

724

3.4.3. Grain nucleation related to strain accumulation

725

726

727

728

729

730

731

732

733

734

Strain building during growth has a high impact on the generation of dislocations but it is also associated to spontaneous new grain nucleation. In the experiment shown in Figures 8.a-b, after twin nucleation, the grain boundary formation at the encounter of twins coming from both sides continues regularly until a new grain nucleates in the grain boundary groove. This grain nucleation event happens regularly at the encounter between twin grains and the central grains. The nucleation of grain α (Figures 8.a and 9) is of particular interest. This grain has a different crystallographic orientation compared to the seed and to the twins on the right and left as evidenced by the topograph in Figure 8.a and by the inverse pole figure map in Figure 9.a. However, it is a twinned grain that nucleated on the left $\{111\}$ facet of the grain boundary groove as shown by the $\Sigma 3$ twin boundary on its left hand side (Figure 9.b).

735

736

737

738

739

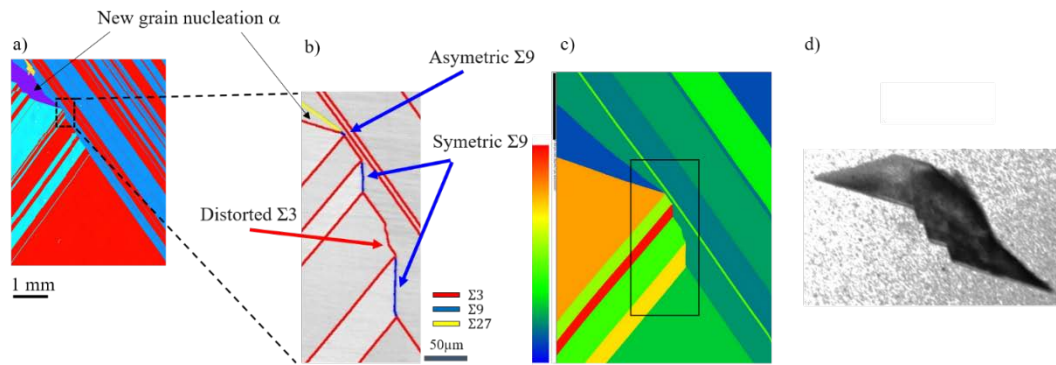
740

741

742

743

Several phenomena are at the origin of the nucleation of this particular grain at the level of the grain boundary groove. The first reason is that the undercooling inside a grain boundary groove is higher than at the level of the solid-liquid interface as discussed in section 3.1 and in our previous work [48] which facilitates grain nucleation in this area. However, it is not a sufficient reason to explain the nucleation at this particular instant as a grain boundary groove was repeatedly formed at the encounter between twins nucleating from the left and right during the experiment. In fact, the grain competition dynamics imposes the formation of twin boundaries non-symmetric or of distorted grain boundaries and induces at the same time accumulation of crystal structure deformation both described in the following for this particular experiment.



744

745

746

747

Figure 9: (a) Inverse Pole Figure (IPF) map along the growth direction (same experiment as in Figures 2, 5.a, 6.a and 8.a-b), (b) high resolution CSL map of the competition region, (c) GOS map of the region of the new nucleated grain (α), (d) Topograph of the grain (α).

748

749

750

751

752

753

754

755

756

757

758

759

760

761

762

763

764

765

766

767

The growth dynamic competition between twin grains coming from the left and right leads to the formation of a distorted $\Sigma 3$ twin boundary (Figure 9.b) at first twin encounter. This distorted $\Sigma 3$ twin boundary gradually evolves to the ideal orientation and straightness of a symmetric $\{111\}$ $\Sigma 3$ twin boundary during growth. Besides, due to the relative crystallographic orientations of the twin grains, $\Sigma 3$ and $\Sigma 9$ twin boundaries are alternately formed. Due to the competition and growth dynamics, some of the $\Sigma 9$ are forced to adopt an asymmetric configuration $\{111\}/\{115\}$ (Figure 9.b). The $\Sigma 9$ twin boundary asymmetric configuration corresponds to a higher grain boundary energy [94]. In fact, it was reported by TEM (Transmission Electron Microscopy) studies coupled to DFT (Density Functional Theory) [94] that on the contrary to the $\Sigma 9 \{122\}_{1,2}$ grain boundary, the atomic structure of the asymmetric $\Sigma 9 \{111\}/\{115\}$ one shows strong distortions. Its energy is about twice as high as that of the symmetric $\Sigma 9 \{122\}_{1,2}$. As a consequence, this situation is unstable from an energetic point of view and not favourable. Just before the nucleation of grain α , at the level of the encounter with a new twin grain from the right, a tiny asymmetric $\Sigma 9 \{111\}/\{115\}$ twin boundary is created. As seen above, non-symmetrical grain boundaries are deformed at the atomic scale [94] and offer greater resistance for dislocation crossing, thereby creating higher strain [92] and structure deformation, promoting dislocation emission. Indeed, the competition goes along with an increasing accumulation of strain when $\Sigma 9$ twin boundaries are present which is revealed by both diffraction images *in situ* during growth and grain orientation spread map (GOS) determined from *ex situ* EBSD measurements after cooling down of the sample (Figure 9.c).

768

769

770

771

772

773

774

775

776

777

778

779

The nucleation in presence of strain accumulation can be triggered by energetic reasons as well as by the existence of the associated dislocations [46]. Indeed, dislocations can favour nucleation by decreasing the nucleation undercooling as discussed in section 3.1. On Figure 9.d showing a topograph corresponding to grain α , it can be seen that the highest strain level (darker contrast) is localized at the position of its nucleation and beginning of its growth. During its growth, the strain level decreases as evidenced by the lighter contrast on the top left side (Figure 9.d). However, inside the grain α , local strain and dislocation emission are observed on the right upper region (Figure 9.d). It is due to another phenomenon namely, to the competition between grains on the right and this newly nucleated grain that tends to extend in the solidification direction. Due to the relative crystallographic orientations of both grains, a $\Sigma 27$ twin boundary is formed. This type of twin boundary is prone to crystal structure deformation and associated dislocation emission as seen above and in [38, 95].

780

781

782

783

784

785

Generally, the new type α grain nucleation contributes to obtain a better crystalline quality in the upper part of the ingot. A lower strain level is observed in the upper growing grains as can be seen in the GOS map (Figure 9.c). Grains above this nucleation event are generally less deformed at the scale of the grain structure and more locally inside the grain that nucleated (Figure 9.d). Strain redistribution cannot be invoked in our experimental case as the existing strain field built during growth remains localised. Yet, the nucleation of grain α did contribute to a lower strain level in the following of growth. In summary, the nucleation can be triggered by energetic reasons discussed

786 above, by grain competition space constraints as well as by the existence of a high density of
787 dislocations that can favour nucleation by decreasing the nucleation undercooling value. This result
788 can be generalized because in other samples with the same crystallographic orientation, processed
789 under similar conditions, comparable grain structures and similar nucleation events to those of grain
790 α are observed. It is worth noting that the nucleation of grain type α is never observed at early growth
791 stages but later during growth when strain has accumulated.

792 Besides, despite the subsequent deformations that can be expected and that are observed at the
793 scale of the sample during cooling down [46], the local strain variations created during growth and
794 due to grain nucleation, competition and strain building during growth are retrieved after cooling
795 down as can be seen on the GOS map that was recorded *ex situ* and with rocking curve imaging in
796 our previous work [38]. These deformed regions remain in the material and can be already associated
797 to dislocations but can be at the origin of further dislocation emissions in subsequent steps of the
798 solar cell fabrication process.

799 4. Conclusions

800 The combination of X-ray radiography and topography imaging achieved *in situ* during the
801 solidification of Si using the GaTSBI tool has proven its efficiency to unveil crystal growth
802 mechanisms. Time-resolved phenomena that occur during crystal growth such as grain nucleation,
803 grain competition, twin formation, defect generation and their evolution and interaction with grains
804 are followed and investigated in real time.

805 The growth of {111} facets at grain boundary grooves and at the edges of the sample was
806 investigated. Nucleation of twin crystals are found to occur preferentially on {111} facets at the edges
807 of the sample where solid – liquid – vapor triple point lines exist and at the location where the sample
808 is in contact with the crucible as well. Nucleation can also take place at the level of {111} facets in
809 grain boundary grooves formed by a grain boundary at the solid-liquid interface. In our growth
810 parameter range, the undercooling at the level of {111} facets at the edges and in grain boundary
811 grooves is always lower than 1 K relatively to the solid-liquid interface, which is sufficient for twin
812 nucleation. Since the undercooling on facets at the edges is higher than the undercooling on facets
813 inside grain boundary grooves, there is a higher nucleation probability at the edges resulting in
814 regular and successive twinning from the sides. Additionally, when studying the {111} facet growth
815 laws, it appears that the experimental results can only be compared reasonably to the quadratic
816 growth law which relies on the presence of dislocations that enhances growth which is highly
817 probable considering other experimental results revealing the presence of dislocations during growth.

818 Moreover, we show that twinning observed with our processing conditions is a growth rather
819 than a deformation phenomenon. Only $\Sigma 3$ twins nucleate during growth, higher order grain
820 boundaries being solely the result of grain competition. One consequence is that the majority of the
821 grain boundaries in the solidified ingot are of $\Sigma 3$ types in samples grown from pure monocrystalline
822 seeds at least while the competition effect is not dominant. The competition and formation of higher
823 order twin boundaries go along with deformations and the accumulation of dislocations. The
824 dislocation behaviour when encountering grain boundaries varies according to the types of grain
825 boundaries. Lower or no dislocation accumulation and deformation are observed at the level of $\Sigma 3$
826 twin boundaries. Indeed, there is a higher probability that dislocations can move along $\Sigma 3$ twin
827 boundaries due to the {111} common glide planes that exists at the level of $\Sigma 3$ twin boundaries
828 compared to the case of higher order twin boundaries. Strain is observed in all cases at the level of
829 higher order twin boundaries either because cross-slip of dislocations is not possible and/or because
830 they are responsible for the emission of dislocations as observed in particular for $\Sigma 27a$ $\langle 110 \rangle$ grain
831 boundaries. Such accumulation can be at the origin of significant crystal structure deformations in
832 the samples. Specifically, areas in which $\Sigma 27a$ $\langle 110 \rangle$ grain boundaries are present are more distorted
833 than the average distortion of the sample. It was also observed that dislocations are emitted at the
834 level of $\Sigma 27a$ $\langle 111 \rangle$ grain boundary. On top of that, the character of the grain boundary (coherent –
835 incoherent) and its Σ – type, its deviation from the optimum orientation and the symmetry or non-

836 symmetry of the boundary planes have an impact on the distortion of the formed boundary and on
837 the emission of dislocations in the vicinity of the surrounding grains as well.

838 Strain building during growth has a high impact on the generation of dislocations but it is also
839 associated with spontaneous grain nucleation. This kind of nucleation event contributes to the
840 recovery of a lower strain level in the upper growing grains. The nucleation in presence of strain
841 accumulation can be triggered by energetic reasons as well as by the existence of associated
842 dislocations. Indeed, dislocations can favour nucleation by decreasing the nucleation undercooling.
843 Another main result is that local strain at the grain scale, which is revealed and monitored during
844 solidification, is retrieved in the ingot after cooling down even though additional strain is created by
845 the cooling down step. However, no detectable additional twin nucleation is observed during cooling
846 down.

847 The enhancement of the recording frequency now provides the opportunity to study the
848 propagation, multiplication and rearrangement of dislocations by interactions with themselves, grain
849 boundaries and the solid-liquid interface, during the whole process. This includes dislocation
850 generation and motion in the seed crystal at high temperature up to the melting point as well as
851 dislocation multiplication and rearrangement during melting, solidification and cooling. In the future,
852 further experiments will be conducted to develop and deepen the investigation of these phenomena.
853 Our work clearly shows that local strain can be built during growth and the synchronisation of X-ray
854 radiography and Bragg diffraction imaging (topography) will allow an enhanced monitoring of strain
855 building. The impact of impurities is not discussed in details in the present manuscript. However,
856 the effect of carbon, oxygen and metallic impurities on grain nucleation and competition is in
857 progress as this is an essential aspect for industrial processes.

858 **Supplementary Materials:** Video S1: Video of radiographs showing the dynamic evolution of the solid-liquid
859 interface during the experiment corresponding to Figures 2, 5.a and 6.a, Video S2: Video of topographs showing
860 twinning and strain formation during solidification in the experiment corresponding to Figure 3.

861 **Author Contributions:** “Conceptualization, N.M, G.R.1, G.R.2., L.B., J.B.; methodology, N.M., G.R.1, G.R.2.;
862 validation, N.M, G.R.1, G.R.2., I.P., J.B.; formal analysis, N.M, G.R.1, G.R.2., J.B., M.B., H.O., T.R.B, M.T.,V.S.,
863 F.G., L.B., I.P.; investigation, N.M, G.R.1, G.R.2., M.B., H.O., T.R.B, M.T.; resources, J.P.V., A.R., E.B., L.B., F.G.;
864 data curation, N.M; writing—original draft preparation, N.M.; writing—review and editing, N.M.;
865 visualization, M.B., H.O., T.R.B, M.T.,V.S., F.G.; supervision, N.M.; project administration, N.M.; funding
866 acquisition, N.M., M.B. All authors have read and agreed to the published version of the manuscript.”

867 **Funding:** This research was funded by Agence Nationale de la Recherche (grant No. 14-CE05-0046-01, CrySaLID
868 project) and Deutsche Forschungsgemeinschaft (scholarship No. BE 6627/1-1 to Maike Becker).

869 **Acknowledgments:** The ESRF (European Synchrotron Radiation Facility) BM05 team is acknowledged for
870 support during some of the X-ray imaging experiments presented in this manuscript.

871 **Conflicts of Interest:** “The authors declare no conflict of interest.”

872 References

- 873 1. Usami, N.; Takahashi, I.; Kutsukake, K.; Fujiwara, K.; Nakajima, K., Implementation of faceted
874 dendrite growth on floating cast method to realize high-quality multicrystalline Si ingot for solar cells.
875 Journal of applied physics 2011, 109 (8), 083527.
- 876 2. Fujiwara, K.; Pan, W.; Usami, N.; Sawada, K.; Tokairin, M.; Nose, Y.; Nomura, A.; Shishido, T.;
877 Nakajima, K., Growth of structure-controlled polycrystalline silicon ingots for solar cells by casting. Acta
878 Materialia 2006, 54 (12), 3191-3197.
- 879 3. Jouini, A.; Ponthenier, D.; Lignier, H.; Enjalbert, N.; Marie, B.; Drevet, B.; Pihan, E.; Cayron, C.;
880 Lafford, T.; Camel, D., Improved multicrystalline silicon ingot crystal quality through seed growth for high
881 efficiency solar cells. Progress in Photovoltaics: Research and Applications 2012, 20, 735-746.
- 882 4. Oliveira, V. A.; Marie, B.; Cayron, C.; Marinova, M.; Tsoutsouva, M. G.; Sio, H. C.; Lafford, T. A.;
883 Baruchel, J.; Audoit, G.; Grenier, A.; Tran Thi, T. N.; Camel, D., Formation mechanism and properties
884 of twinned structures in (111) seeded directionally solidified solar grade silicon. Acta Materialia 2016, 121,
885 24-36.

- 886 5. Stoddard, N.; Wu, B.; Witting, I.; Wagener, M. C.; Park, Y.; Rozgonyi, G. A.; Clark, R., Casting Single
887 Crystal Silicon: Novel Defect Profiles from BP Solar's Mono2™ Wafers. *Solid State Phenomena* 2008, 131-
888 133, 1-8.
- 889 6. Lan, C. W.; Lan, A.; Yang, C. F.; Hsu, H. P.; Yang, M.; Yu, A.; Hsu, B.; Hsu, W. C.; Yang, A., The
890 emergence of high-performance multi-crystalline silicon in photovoltaics. *Journal of Crystal Growth* 2017,
891 468, 17-23.
- 892 7. Trempa, M.; Reimann, C.; Friedrich, J.; Müller, G.; Oriwol, D., Mono-crystalline growth in directional
893 solidification of silicon with different orientation and splitting of seed crystals. *Journal of Crystal Growth*
894 2012, 351, 131-140.
- 895 8. Oliveira, V. A.; Rocha, M.; Lantreibecq, A.; Tsoutsouva, M. G.; Tran-Thi, T. N.; Baruchel, J.; Camel,
896 D., Cellular dislocations patterns in monolike silicon: Influence of stress, time under stress and impurity
897 doping. *Journal of Crystal Growth* 2018, 489, 42-50.
- 898 9. Tsoutsouva, M. G.; Oliveira, V. A.; Camel, D.; Baruchel, J.; Marie, B.; Lafford, T. A., Mono-like silicon
899 ingots grown on low angle misoriented seeds: Defect characterization by synchrotron X-ray diffraction
900 imaging. *Acta Materialia* 2015, 88 (0), 112-120.
- 901 10. Tsoutsouva, M. G.; Oliveira, V. A.; Camel, D.; Tran Thi, T. N.; Baruchel, J.; Marie, B.; Lafford, T. A.,
902 Segregation, precipitation and dislocation generation between seeds in directionally solidified mono-like
903 silicon for photovoltaic applications. *Journal of Crystal Growth* 2014, 401 (0), 397-403.
- 904 11. Ekstrøm, K. E.; Stokkan, G.; Søndena, R.; Dalaker, H.; Lehmann, T.; Arnberg, L.; Di Sabatino, M.,
905 Structure and dislocation development in mono-like silicon. *physica status solidi (a)* 2015, 212 (10), 2278-
906 2288.
- 907 12. Autruffe, A.; Stenhjem Hagen, V.; Arnberg, L.; Di Sabatino, M., Dislocation generation at near-
908 coincidence site lattice grain boundaries during silicon directional solidification. *Journal of Crystal Growth*
909 2015, 411, 12-18.
- 910 13. Autruffe, A.; Vines, L.; Arnberg, L.; Di Sabatino, M., Coincident site lattice bi-crystals growth—Impurity
911 segregation towards grain boundaries. *Journal of Crystal Growth* 2015, 416, 8-11.
- 912 14. Trempa, M.; Reimann, C.; Friedrich, J.; Müller, G.; Sylla, L.; Krause, A.; Richter, T., Investigation of
913 iron contamination of seed crystals and its impact on lifetime distribution in Quasimono silicon ingots.
914 *Journal of Crystal Growth* 2015, 429, 56-62.
- 915 15. Trempa, M.; Reimann, C.; Friedrich, J.; Müller, G.; Krause, A.; Sylla, L.; Richter, T., Influence of
916 grain boundaries intentionally induced between seed plates on the defect generation in quasi-mono-
917 crystalline silicon ingots. *Crystal Research and Technology* 2015, 50 (1), 124-132.
- 918 16. Trempa, M.; Reimann, C.; Friedrich, J.; Müller, G.; Krause, A.; Sylla, L.; Richter, T., Defect formation
919 induced by seed-joints during directional solidification of quasi-mono-crystalline silicon ingots. *Journal of*
920 *Crystal Growth* 2014, 405 (0), 131-141.
- 921 17. Stokkan, G.; Song, A.; Rynningen, B., Investigation of the Grain Boundary Character and Dislocation
922 Density of Different Types of High Performance Multicrystalline Silicon. *Crystals* 2018, 8 (9), 341.
- 923 18. Hurler, D. T. J., A mechanism for twin formation during Czochralski and encapsulated vertical Bridgman
924 growth of III-V compound semiconductors. *Journal of Crystal Growth* 1995, 147 (3), 239-250.
- 925 19. von Ammon, W., FZ and CZ crystal growth: Cost driving factors and new perspectives. *physica status*
926 *solidi (a)* 2014, 211 (11), 2461-2470.
- 927 20. Oliveira, V. A.; Sio, H. C.; Faujour, A.; Piot, L.; Chabli, A.; Camel, D., Recombination Activity of 2D
928 Extended Defects in Monolike Silicon. *Energy Procedia* 2016, 92, 755-763.
- 929 21. Woo, S.; Bertoni, M.; Choi, K.; Nam, S.; Castellanos, S.; Powell, D. M.; Buonassisi, T.; Choi, H., An
930 insight into dislocation density reduction in multicrystalline silicon. *Solar Energy Materials and Solar Cells*
931 2016, 155, 88-100.
- 932 22. Wang, Z.-J.; Tsurekawa, S.; Ikeda, K.; Sekiguchi, T.; Watanabe, T., Relationship between Electrical
933 Activity and Grain Boundary Structural Configuration in Polycrystalline Silicon. *Interface Sci* 1999, 7 (2),
934 197-205.
- 935 23. Fedotov, A.; Evtodiy, B.; Fionova, L.; Ilyashuk, Y.; Katz, E.; Polyak, L., Electrical-Activity of Grain-
936 Boundaries in Shaped Grown Silicon. *Phys Status Solidi A* 1990, 119 (2), 523-534.
- 937 24. Kivambe, M.; Ervik, T.; Rynningen, B.; Stokkan, G., On the role of stacking faults on dislocation
938 generation and dislocation cluster formation in multicrystalline silicon. *Journal of Applied Physics* 2012,
939 112, 103528.

- 940 25. Binetti, S.; Libal, J.; Acciarri, M.; Di Sabatino, M.; Nordmark, H.; Øvrelid, E. J.; Walmsley, J. C.;
941 Holmestad, R., Study of defects and impurities in multicrystalline silicon grown from metallurgical silicon
942 feedstock. *Materials Science and Engineering: B* 2009, 159–160 (0), 274–277.
- 943 26. Oriwol, D.; Carl, E. R.; Danilewsky, A. N.; Sylla, L.; Seifert, W.; Kittler, M.; Leipner, H. S., Small-
944 angle subgrain boundaries emanating from dislocation pile-ups in multicrystalline silicon studied with
945 synchrotron white-beam X-ray topography. *Acta Materialia* 2013, 61 (18), 6903–6910.
- 946 27. Adamczyk, K.; Søndena, R.; Stokkan, G.; Looney, E.; Jensen, M.; Lai, B.; Rinio, M.; Sabatino, M. D.,
947 Recombination activity of grain boundaries in high-performance multicrystalline Si during solar cell
948 processing. *Journal of applied physics* 2018, 123 (5), 055705.
- 949 28. Wang, H. Y.; Usami, N.; Fujiwara, K.; Kutsukake, K.; Nakajima, K., Microstructures of Si multicrystals
950 and their impact on minority carrier diffusion length. *Acta Materialia* 2009, 57 (11), 3268–3276.
- 951 29. Autruffe, A.; Søndena, R.; Vines, L.; Arnberg, L.; Di Sabatino, M., Influence of pulling rate on
952 multicrystalline silicon ingots' properties. *Journal of Crystal Growth* 2014, 386 (0), 199–203.
- 953 30. Duffar, T., Comprehensive review on grain and twin structures in bulk photovoltaic silicon. *Recent*
954 *Research Developments Crystal Growth* 2009, 5, 61–111.
- 955 31. Gallien, B.; Duffar, T.; Lay, S.; Robaut, F., Analysis of grain orientation in cold crucible continuous casting
956 of photovoltaic Si. *Journal of Crystal Growth* 2011, 318, 208–211.
- 957 32. Lan, C. W.; Lan, W. C.; Lee, T. F.; Yu, A.; Yang, Y. M.; Hsu, W. C.; Hsu, B.; Yang, A., Grain control
958 in directional solidification of photovoltaic silicon. *Journal of Crystal Growth* 2012, 360, 68–75.
- 959 33. Reimann, C.; Müller, G.; Friedrich, J.; Lauer, K.; Simonis, A.; Wätzig, H.; Krehan, S.; Hartmann,
960 R.; Kruse, A., Systematic characterization of multi-crystalline silicon String Ribbon wafer. *Journal of Crystal*
961 *Growth* 2012, 361 (0), 38–43.
- 962 34. Zhou, N.; Wei, X.; Zhou, L., Formation of Dislocations in the Growth of Silicon along Different
963 Crystallographic Directions—A Molecular Dynamics Study. *Crystals* 2018, 8 (9), 346.
- 964 35. Fujiwara, K.; Maeda, K.; Usami, N.; Sazaki, G.; Nose, Y.; Nomura, A.; Shishido, T.; Nakajima, K.,
965 In situ observation of Si faceted dendrite growth from low-degree-of-undercooling melts. *Acta Materialia*
966 2008, 56 (11), 2663–2668.
- 967 36. Fujiwara, K.; Obinata, Y.; Ujihara, T.; Usami, N.; Sazaki, G.; Nakajima, K., Grain growth behaviors of
968 polycrystalline silicon during melt growth processes. *Journal of Crystal Growth* 2004, 266 (4), 441–448.
- 969 37. Ribéri-Béridot, T.; Mangelinck-Noël, N.; Tandjaoui, A.; Reinhart, G.; Billia, B.; Lafford, T.;
970 Baruchel, J.; Barrallier, L., On the impact of twinning on the formation of the grain structure of multi-
971 crystalline silicon for photovoltaic applications during directional solidification. *Journal of Crystal Growth*
972 2015, 418, 38–44.
- 973 38. Tsoutsouva, M. G.; Ribéri – Béridot, T.; Regula, G.; Reinhart, G.; Baruchel, J.; Guittonneau, F.;
974 Barrallier, L.; Mangelinck-Noël, N., In situ investigation of the structural defect generation and evolution
975 during the directional solidification of <110> seeded growth Si. *Acta Materialia* 2016, 115, 210–223.
- 976 39. Chuang, L.-C.; Maeda, K.; Morito, H.; Shiga, K.; Miller, W.; Fujiwara, K., In situ observation of
977 interaction between grain boundaries during directional solidification of Si. *Scripta Materialia* 2018, 148,
978 37–41.
- 979 40. Nagashio, K.; Adachi, M.; Higuchi, K.; Mizuno, A.; Watanabe, M.; Kuribayashi, K.; Katayama, Y.,
980 Real-time x-ray observation of solidification from undercooled Si melt. *Journal of Applied Physics* 2006,
981 100 (3).
- 982 41. Nagashio, K.; Murata, H.; Kuribayashi, K., In situ observation of solidification behavior of Si melt
983 dropped on Si wafer by IR thermography. *Journal of Crystal Growth* 2005, 275, e1685–e1690.
- 984 42. Fujiwara, K.; Maeda, K.; Usami, N.; Sazaki, G.; Nose, Y.; Nakajima, K., Formation mechanism of
985 parallel twins related to Si-faceted dendrite growth. *Scripta Materialia* 2007, 57, 81–84.
- 986 43. Fujiwara, K.; Nakajima, K.; Ujihara, T.; Usami, N.; Sazaki, G.; Hasegawa, H.; Mizoguchi, S.;
987 Nakajima, K., In situ observations of crystal growth behavior of silicon melt. *Journal of Crystal Growth*
988 2002, 243 (2), 275–282.
- 989 44. Chikawa, J.-I., Technique for the video display of X-ray topographic images and its application to the study
990 of crystal growth. *Journal of Crystal Growth* 1974, 24–25, 61–68.
- 991 45. Chikawa, J.-i.; Shirai, S., Melting of silicon crystals and a possible origin of swirl defects. *Journal of Crystal*
992 *Growth* 1977, 39 (2), 328–340.

- 993 46. Riberi – Béridot, T.; Tsoutsouva, M. G.; Regula, G.; Reinhart, G.; Guittonneau, F.; Barrallier, L.;
994 Mangelinck-Noël, N., Strain building and correlation with grain nucleation during silicon growth. *Acta*
995 *Materialia* 2019, 177, 141-150.
- 996 47. Riberi-Béridot, T.; Tsoutsouva, M. G.; Regula, G.; Reinhart, G.; Périchaud, I.; Baruchel, J.;
997 Mangelinck-Noël, N., Growth undercooling in multi-crystalline pure silicon and in silicon containing light
998 impurities (C and O). *Journal of Crystal Growth* 2017, 466, 64-70.
- 999 48. Stamelou, V.; Tsoutsouva, M. G.; Riberi-Béridot, T.; Reinhart, G.; Regula, G.; Baruchel, J.;
1000 Mangelinck-Noël, N., {111} facet growth laws and grain competition during silicon crystallization. *Journal*
1001 *of Crystal Growth* 2017, 479, 1-8.
- 1002 49. Riberi-Béridot, T.; Mangelinck-Noël, N.; Tandjaoui, A.; Reinhart, G.; Billia, B.; Lafford, T.;
1003 Baruchel, J.; Barrallier, L., On the impact of twinning on the formation of the grain structure of multi-
1004 crystalline silicon for photovoltaic applications during directional solidification. *Journal of Crystal Growth*
1005 2015, 418 (0), 38-44.
- 1006 50. Tandjaoui, A.; Mangelinck-Noël, N.; Reinhart, G.; Billia, B.; Furter, J. J.; Lafford, T.; Baruchel, J.;
1007 Guichard, X., Real time observation of the directional solidification of multicrystalline silicon: X-ray
1008 imaging characterization. *Energy Procedia* 2012, 27, 82-87.
- 1009 51. Tandjaoui, A.; Mangelinck-Noël, N.; Reinhart, G.; Billia, B.; Guichard, X., Twinning occurrence and
1010 grain competition in multicrystalline silicon during solidification. *C.R. Physique* 2013, 14, 8.
- 1011 52. Tandjaoui, A.; Mangelinck-Noël, N.; Reinhart, G.; Billia, B.; Lafford, T.; Baruchel, J., Investigation of
1012 grain boundary grooves at the solid-liquid interface during directional solidification of multi-crystalline
1013 silicon: in situ characterization by X-ray imaging. *Journal of Crystal Growth* 2013, 377, 203-211.
- 1014 53. Becker, M.; Regula, G.; Reinhart, G.; Boller, E.; Valade, J.-P.; Rack, A.; Tafforeau, P.; Mangelinck-
1015 Noel, N., Simultaneous X-ray radiography and diffraction topography imaging applied to silicon for defect
1016 analysis during melting and crystallization. *Journal of Applied Crystallography* 2019, 52 (6), 1312-1320.
- 1017 54. Ouaddah, H.; Périchaud, I.; Barakel, D.; Palais, O.; Di Sabatino, M.; Reinhart, G.; Regula, G.;
1018 Mangelinck-Noël, N., Role of Impurities in Silicon Solidification and Electrical Properties Studied by
1019 Complementary In Situ and Ex Situ Methods. *physica status solidi (a)* 2019, 1900298, 1-10.
- 1020 55. Baruchel, J.; Buffiere, J.-Y.; Cloetens, P.; Di Michiel, M.; Ferrie, E.; Ludwig, W.; Maire, E.; Salvo, L.,
1021 Advances in synchrotron radiation microtomography. *Scripta Materialia* 2006, 55 (1), 41-46.
- 1022 56. Cloetens, P.; Barrett, R.; Baruchel, J.; Guigay, J.-P.; Schlenker, M., Phase objects in synchrotron
1023 radiation hard x-ray imaging. *Journal of Physics D: Applied Physics* 1996, 29 (1), 133-146.
- 1024 57. Reinhart, G.; Grange, D.; Abou-Khalil, L.; Mangelinck-Noël, N.; Niane, N. T.; Maguin, V.;
1025 Guillemot, G.; Gandin, C. A.; Nguyen-Thi, H., Impact of solute flow during directional solidification of a
1026 Ni-based alloy: in-situ and real-time X-radiography. *Acta Materialia* 2020.
- 1027 58. Schneider, C. A.; Rasband, W. S.; Eliceiri, K. W., NIH Image to ImageJ: 25 years of image analysis. *Nat.*
1028 *Methods* 2012, 9 (7), 671-675.
- 1029 59. Härtwig, J., Hierarchy of dynamical theories of x-ray diffraction for deformed and perfect crystals. *Journal*
1030 *of Physics D: Applied Physics* 2001, 34 (10A), A70-A77.
- 1031 60. Mittone, A.; Manakov, I.; Broche, L.; Jarnias, C.; Coan, P.; Bravin, A., Characterization of a sCMOS-
1032 based high-resolution imaging system. *Journal of Synchrotron Radiation* 2017, 24 (6), 1226-1236.
- 1033 61. Lang, A. R., The early days of high-resolution X-ray topography. *Journal of Physics D: Applied Physics*
1034 1993, 26 (4A), A1-A8.
- 1035 62. Burns, R. C.; Chumakov, A. I.; Connell, S. H.; Dube, D.; Godfried, H. P.; Hansen, J. O.; Härtwig, J.;
1036 Hozzowska, J.; Masiello, F.; Mkhonza, L.; Rebak, M.; Rommevaux, A.; Setshedi, R.; Vaerenbergh, P.
1037 V., HPHT growth and x-ray characterization of high-quality type IIa diamond. *Journal of Physics:*
1038 *Condensed Matter* 2009, 21 (36), 364224.
- 1039 63. Authier, A., Contrast of Dislocation Images in X-Ray Transmission Topography. *Advances in X-ray*
1040 *Analysis* 1966, 10, 9-31.
- 1041 64. De Graef, M.; McHenry, M. E., *Structure of materials: an introduction to crystallography, diffraction and*
1042 *symmetry*. 2007.
- 1043 65. Danilewsky, A. N.; Wittge, J.; Croell, A.; Allen, D.; McNally, P.; Vagovič, P.; dos Santos Rolo, T.;
1044 Li, Z.; Baumbach, T.; Gorostegui-Colinas, E.; Garagorri, J.; Elizalde, M. R.; Fossati, M. C.; Bowen,
1045 D. K.; Tanner, B. K., Dislocation dynamics and slip band formation in silicon: In-situ study by X-ray
1046 diffraction imaging. *Journal of Crystal Growth* 2011, 318 (1), 1157-1163.

- 1047 66. Vallino, F.; Chateau, J. P.; Jacques, A.; George, A., Dislocation multiplication during the very first stages
1048 of plastic deformation in silicon observed by X-ray topography. *Mat Sci Eng a-Struct* 2001, 319, 152-155.
- 1049 67. Danilewsky, A.; Wittge, J.; Kiefl, K.; Allen, D.; McNally, P.; Garagorri, J.; Elizalde, M. R.;
1050 Baumbach, T.; Tanner, B. K., Crack propagation and fracture in silicon wafers under thermal stress. *Journal*
1051 *of applied crystallography* 2013, 46 (Pt 4), 849-855.
- 1052 68. Lafford, T. A.; Villanova, J.; Plassat, N.; Dubois, S.; Camel, D., Synchrotron X-ray imaging applied to
1053 solar photovoltaic silicon. *Journal of Physics: Conference Series* 2013, 425 (19), 192019.
- 1054 69. Yao, Y.; Sugawara, Y.; Ishikawa, Y., Observation of dislocations in β -Ga₂O₃ single-crystal substrates by
1055 synchrotron X-ray topography, chemical etching, and transmission electron microscopy. *Japanese Journal*
1056 *of Applied Physics* 2020, 59 (4), 045502.
- 1057 70. Lantreibecq, A.; Monchoux, J. P.; Pihan, E.; Marie, B.; Legros, M., Subgrains, micro-twins and
1058 dislocations characterization in monolike Si using TEM and in-situ TEM. *Materials Today: Proceedings*
1059 2018, 5 (6, Part 3), 14732-14747.
- 1060 71. Qiang, Z.; Peizhen, D.; Fuxi, G., X-ray topographic observation of dislocation structure in sapphire single
1061 crystal grown by temperature gradient technique. *Journal of Crystal Growth* 1991, 108 (1), 377-384.
- 1062 72. Tsoutsouva, M. G.; Riberi – Béridot, T.; Regula, G.; Reinhart, G.; Baruchel, J.; Mangelinck-Noël, N., In
1063 Situ Imaging of Dislocation Expansion in FZ-Si Seeds During Temperature Ramp Heating Process. *Physica*
1064 *status solidi (a)* 2018, A, 1700758.
- 1065 73. Miller, W., Some remarks on the undercooling of the Si(111) facet and the “Monte Carlo modeling of silicon
1066 crystal growth” by Kirk M. Beatty & Kenneth A. Jackson, J. *Crystal Growth* 211 (2000) 13. *Journal of Crystal*
1067 *Growth* 2011, 325 (1), 101-103.
- 1068 74. Voronkov, V. V., Supercooling at the facet developing on a rounded crystalization front. *Soviet Physics -*
1069 *Crystallography* 1973, 17 (5), 807-813.
- 1070 75. Nadri, A.; Duterrail-Couvat, Y.; Duffar, T., Two-dimensional numerical modeling of grain structure in
1071 multi-crystalline silicon ingot. *Journal of Crystal Growth* (0).
- 1072 76. Lin, H. K.; Lan, C. W., Phase field modeling of grain structure evolution during directional solidification of
1073 multi-crystalline silicon sheet. *Journal of Crystal Growth* 2017, 475, 150-157.
- 1074 77. Pineau, A.; Guillemot, G.; Reinhart, G.; Regula, G.; Mangelinck-Noël, N.; Gandin, C. A., Three-
1075 dimensional cellular automaton modeling of silicon crystallization with grains in twin relationships. *Acta*
1076 *Materialia* 2020.
- 1077 78. Coriell, S. R.; Sekerya, R. F., Morphological stability near a grain boundary groove in a solid-liquid interface
1078 during solidification of a binary alloy. *Journal of Crystal Growth* 1973, 19 (4), 285-293.
- 1079 79. Duffar, T.; Nadri, A., The grain–grain–liquid triple phase line during solidification of multi-crystalline
1080 silicon. *Comptes Rendus Physique* 2013, 14 (2–3), 185-191.
- 1081 80. Tandjaoui, A.; Mangelinck-Noël, N.; Reinhart, G.; Billia, B.; Lafford, T.; Baruchel, J., Investigation of
1082 grain boundary grooves at the solid-liquid interface during directional solidification of high purity silicon:
1083 characterization in situ by X-ray imaging. *Journal of Crystal Growth* 2013, 377, 203-211.
- 1084 81. Jackson, K. A., *Crystal Growth Kinetics. Materials Science & Engineering* 1984, 65, 7-13.
- 1085 82. Dash, J. G.; Hodgkin, V. A.; Wettlaufer, J. S., Dynamics of Faceted Grain Boundary Grooves. *Journal of*
1086 *Statistical Physics* 1999, 95 (5/6), 1311-1322.
- 1087 83. Ervik, T.; Stokkan, G.; Buonassisi, T.; Mjøs, Ø.; Lohne, O., Dislocation formation in seeds for quasi-
1088 monocrystalline silicon for solar cells. *Acta Materialia* 2014, 67 (0), 199-206.
- 1089 84. Lin, H. K.; Wu, M. C.; Chen, C. C.; Lan, C. W., Evolution of grain structures during directional
1090 solidification of silicon wafers. *Journal of Crystal Growth* 2016, 439, 40-46.
- 1091 85. Stockmeier, L.; Müller, G.; Seidl, A.; Lehmann, T.; Reimann, C.; Friedrich, J., Preferred grain
1092 orientations in silicon ribbons grown by the string ribbon and the edge-defined film-fed growth methods.
1093 *Journal of Crystal Growth* 2014, 395 (0), 74-79.
- 1094 86. Heilbronn, B.; De Moro, F.; Jolivet, E.; Tupin, E.; Chau, B.; Varrot, R.; Drevet, B.; Bailly, S.; Rey,
1095 D.; Lignier, H.; Xi, Y.; Riberi-Béridot, T.; Mangelinck-Noël, N.; Reinhart, G.; Regula, G., Fast growth
1096 of thin multi-crystalline silicon ribbons by the RST method. *Crystal Research and Technology* 2014, 1-14.
- 1097 87. Mangelinck-Noël, N.; Pihan, E., Le nouveau du silicium dope les panneaux solaires. *La Recherche*
1098 *Septembre* 2018, 2018.
- 1099 88. Jhang, J. W.; Regula, G.; Reinhart, G.; Mangelinck-Noël, N.; Lan, C. W., Heterogeneous twinning
1100 during directional solidification of multi-crystalline silicon. *Journal of Crystal Growth* 2019, 508, 42-49.

- 1101 89. Alexander, H.; Haasen, P., Dislocations and plastic flow in the diamond structure. *Solid State Physics* 1968,
1102 22, 27.
- 1103 90. Takahashi, I.; Usami, N.; Kutsukake, K.; Stokkan, G.; Morishita, K.; Nakajima, K., Generation
1104 mechanism of dislocations during directional solidification of multicrystalline silicon using artificially
1105 designed seed. *Journal of Crystal Growth* 2010, 312 (7), 897-901.
- 1106 91. Rynningen, B.; Stokkan, G.; Kivambe, M.; Ervik, T.; Lohne, O., Growth of dislocation clusters during
1107 directional solidification of multicrystalline silicon ingots. *Acta Materialia* 2011, 59 (20), 7703-7710.
- 1108 92. Lim, R. C.; Raj, R., Interaction between lattice and grain boundary dislocations and their role in mechanical
1109 properties of interfaces. *Journal de Physique Colloques* 1985, 46 (C4), C4-581 - C4-595.
- 1110 93. Brokman, A.; Bristowe, P. D.; Balluffi, R. W., Atomistic faceting of asymmetric tilt boundaries. *Script*
1111 *Metallurgica* 1981, 15, 201-206.
- 1112 94. Stoffers, A.; Ziebarth, B.; Barthel, J.; Cojocaru-Mirédin, O.; Elsässer, C.; Raabe, D., Complex Nanotwin
1113 Substructure of an Asymmetric S9 Tilt Grain Boundary in a Silicon Polycrystal. *Physical Review Letters*
1114 2015, 115 (23), 235502.
- 1115 95. Stokkan, G.; Hu, Y.; Mjøs, Ø.; Juel, M., Study of evolution of dislocation clusters in high performance
1116 multicrystalline silicon. *Sol Energ Mat Sol C* 2014, 130, 679-685.
- 1117



© 2020 by the authors. Submitted for possible open access publication under the terms and conditions of the Creative Commons Attribution (CC BY) license (<http://creativecommons.org/licenses/by/4.0/>).

1118